

# Subseasonal prediction of the state and evolution of the North Pacific jet stream

Andrew Winters<sup>1,1</sup>

<sup>1</sup>University of Colorado Boulder

November 30, 2022

## Abstract

The state and evolution of the North Pacific jet (NPJ) stream strongly influences the character of the downstream synoptic-scale flow pattern over North America. This study employs data from nine models within the Subseasonal-to-Seasonal Reforecast Database hosted by the European Centre for Medium-Range Weather Forecasts to examine the subseasonal (2 weeks–1 month) predictability of the NPJ through the lens of an NPJ phase diagram. The NPJ phase diagram provides a visual representation of the state and evolution of the NPJ with respect to the two leading modes of NPJ variability. The first mode of NPJ variability corresponds to a zonal extension or retraction of the climatological jet-exit region, whereas the second mode corresponds to a poleward or equatorward shift of the climatological jet-exit region. The analysis reveals that ensemble forecasts of the prevailing NPJ regime, as determined from the NPJ phase diagram, are skillful into week 3 of the forecast period. Forecasts initialized during a jet retraction, or verifying during a jet retraction and equatorward shift, feature the largest forecast errors during weeks 1–2 of the forecast period for all models. Beyond week 2, the verifying NPJ regime characterized by the largest forecast error varies by model and is related to forecast frequency biases in the prediction of each NPJ regime at subseasonal time scales. Examination of the worst-performing 21-day forecasts from each model demonstrates that the worst-performing forecasts are uniformly associated with development, maintenance, and decay of upper-tropospheric ridges over the high-latitude North Pacific.

1  
2  
3  
4  
5  
6  
7  
8  
9 **Subseasonal prediction of the state and evolution of the North Pacific jet stream**

10  
11 *By*

12  
13 ANDREW C. WINTERS<sup>1\*</sup>

14  
15  
16  
17 <sup>1</sup>Department of Atmospheric and Oceanic Sciences  
18 University of Colorado Boulder  
19 Boulder, CO 80309  
20

21  
22 Submitted for publication in the  
23 *Journal of Geophysical Research: Atmospheres*  
24 16 April 2021  
25 Revised: 10 August 2021  
26  
27  
28

29 **Keywords:** subseasonal prediction, North Pacific jet stream, weather regimes  
30

31 **Key Points:**

- 32  
33 1) Skillful predictions of the prevailing North Pacific jet regime extend into the week 3  
34 forecast period.  
35 2) Bias-corrected forecasts verifying during jet retraction or equatorward shift regimes  
36 feature the largest errors at subseasonal lead times.  
37 3) The worst 21-day forecasts from each model are associated with the development,  
38 maintenance, and decay of upper-tropospheric ridges.

---

\* *Corresponding author address:* Andrew C. Winters, Dept. of Atmospheric and Oceanic Sciences, University of Colorado Boulder, 311 UCB, Boulder, CO 80309. E-mail: andrew.c.winters@colorado.edu



## Abstract

The state and evolution of the North Pacific jet (NPJ) stream strongly influences the character of the downstream synoptic-scale flow pattern over North America. This study employs data from nine models within the Subseasonal-to-Seasonal Reforecast Database hosted by the European Centre for Medium-Range Weather Forecasts to examine the subseasonal (2 weeks–1 month) predictability of the NPJ through the lens of an NPJ phase diagram. The NPJ phase diagram provides a visual representation of the state and evolution of the NPJ with respect to the two leading modes of NPJ variability. The first mode of NPJ variability corresponds to a zonal extension or retraction of the climatological jet-exit region, whereas the second mode corresponds to a poleward or equatorward shift of the climatological jet-exit region. The analysis reveals that ensemble forecasts of the prevailing NPJ regime, as determined from the NPJ phase diagram, are skillful into week 3 of the forecast period. Forecasts initialized during a jet retraction, or verifying during a jet retraction and equatorward shift, generally feature the largest errors during the forecast period. Examination of the worst-performing 21-day forecasts from each model demonstrates that the worst-performing forecasts are uniformly associated with development, maintenance, and decay of upper-tropospheric ridges over the high-latitude North Pacific. These results demonstrate that bias-corrected NPJ phase diagram forecasts have the potential to identify periods that may exhibit enhanced forecast skill at subseasonal lead times based on the anticipated NPJ evolution.

## **Plain Language Summary**

The jet stream is a ribbon of rapidly moving air that circumnavigates the globe approximately 12 km above the Earth's surface. The evolution of a segment of the jet stream over the North Pacific, hereafter referred to as the North Pacific jet (NPJ), exerts an important influence on downstream weather conditions over North America. Consequently, this study examines the extent to which forecast models can accurately capture the state and evolution of the NPJ 2–4 weeks in advance. The analysis reveals that an elongated or poleward shifted NPJ is generally characterized by enhanced forecast accuracy, whereas a wavier or split NPJ is generally characterized by reduced forecast accuracy. Recognition of these NPJ configurations within a real time forecast environment can provide “windows of opportunity”, in which conditions over the North Pacific and North America can be forecasted with a higher degree of precision compared to climatology up to 4 weeks in advance.

## 1. Introduction

The improvement of subseasonal (2 weeks to 1 month) forecasts has been a priority for the meteorological community and its partners (NRC, 2010; NAS, 2018) given that this time scale is characterized by a forecast skill “gap” within numerical weather prediction models. In particular, skillful forecasts on shorter (i.e., weather) time scales predominantly arise from atmospheric initial conditions, whereas skillful forecasts on longer (i.e., seasonal) time scales predominantly arise from low frequency climate variations such as sea-surface temperature and soil moisture fluctuations (e.g., NRC, 2010; NAS, 2018; Vitart et al., 2017; Pegion et al., 2019; Meehl et al., 2021). Consequently, the subseasonal time scale lies in a transition period during which forecast skill is not as effectively derived from atmospheric initial conditions or low frequency climate variations. Nevertheless, subseasonal forecasts offer considerable value to stakeholders, including individuals in emergency management, agriculture, water management, and public health (White et al., 2017; Pegion et al., 2019), who can act to mitigate risks from the occurrence of anomalous weather conditions.

The identification and prediction of “weather regimes”, which are defined as reoccurring and/or persistent large-scale atmospheric patterns maintained by synoptic-scale weather systems (e.g., Reinhold & Pierrehumbert, 1982; Vautard, 1990; Ferranti et al., 2015, 2018; Straus et al., 2017; Vigaud et al. 2018; Lee et al. 2019; Winters et al. 2019a; Robertson et al., 2020), represent burgeoning areas of research relevant to the subseasonal time scale. Weather regimes can be defined over a spectrum of spatial domains, such as the Northern Hemisphere (e.g., Mo & Ghil, 1988; Kimoto & Ghil, 1993; Corti et al., 1999), the Euro–Atlantic sector (e.g., Vautard, 1990; Michelangeli et al., 1995; Cassou, 2008; Dawson & Palmer, 2014; Ferranti et al., 2015, 2018; Grams et al., 2017; Matsueda & Palmer, 2018), and the Pacific–North American sector (e.g.,

Robertson & Ghil, 1999; Straus et al., 2007; Riddle et al., 2013; Matsueda & Kyouda, 2016; Vigaud et al., 2018; Amini & Straus, 2019; Lee et al., 2019; Winters et al., 2019a; Robertson et al., 2020). Knowledge of the prevailing or forecasted weather regime subsequently provides insight into the character of the large-scale flow pattern over a region as well as the relative likelihood for anomalous sensible weather to develop in conjunction with that regime.

Examinations into the predictability of weather regimes have been predominantly focused on the Euro-Atlantic sector (e.g., Ferranti et al. 2015, 2018; Matsueda & Palmer, 2018). A common thread among these examinations is that forecast models have difficulty capturing the onset, maintenance, and decay of upper-tropospheric blocking events, which has implications for the occurrence of high-impact weather events over Europe, such as cold-air outbreaks and heat waves (e.g., Jung et al., 2011; Ferranti et al., 2018; Quandt et al., 2019). Evaluation of the predictability of weather regimes over North America has recently received greater attention. In particular, Vigaud et al. (2018) and Robertson et al. (2020) demonstrate that the predictability of North American weather regimes, as defined from a *k*-means clustering analysis of 500-hPa geopotential height, is generally on the order of two weeks. Robertson et al. (2020) observe, however, that there are “forecasts of opportunity” in which the prevailing weather regime may be predicted with skill up to four weeks in advance. These forecasts of opportunity were found to coincide with periods influenced by low frequency modes of climate variability such as the El Niño–Southern Oscillation and the Madden–Julian Oscillation.

The North Pacific jet (NPJ) stream represents a synoptic-scale feature whose state and evolution serves as a conduit between the aforementioned modes of low frequency climate variability and the character of the downstream large-scale flow pattern over North America (e.g., Cordeira & Bosart, 2010; Archambault et al., 2015; Bosart et al., 2017; Griffin & Martin,

2017; Vignaud et al. 2018; Winters et al., 2019a,b; Robertson et al., 2020). Therefore, accurate forecasts of the state and evolution of the NPJ may also exhibit the potential to inform predictions of weather conditions over North America. Winters et al. (2019a) developed an NPJ phase diagram on the basis of this observation to objectively track the state and evolution of the NPJ using output from reanalysis products and numerical weather prediction models. The NPJ phase diagram is constructed from the two-leading empirical orthogonal functions (EOFs) of 250-hPa zonal wind anomalies over the North Pacific during September–May. The first EOF corresponds to a zonal extension or retraction of the climatological exit region of the NPJ, whereas the second EOF corresponds to a poleward or equatorward shift of the climatological exit region of the NPJ. Figure 1 shows the characteristic large-scale flow patterns associated with the four primary NPJ regimes derived from the NPJ phase diagram and reveals that each NPJ regime is associated with distinct temperature and sea-level pressure anomaly patterns across the Pacific–North American sector. Winters et al. (2019b) and Turasky (2019) further demonstrate that the frequencies of continental U.S. extreme temperature events and landfalling atmospheric river events along the U.S. west coast are significantly modulated by the antecedent state and evolution of the NPJ as determined from the NPJ phase diagram.

Predicated on the relationship between each NPJ regime and the large-scale flow pattern over North America, Winters et al. (2019a) conducted an evaluation of the medium-range (6–10-day) forecast skill associated with each NPJ regime by calculating 9-day ensemble forecasts of the state and evolution of the NPJ in the context of the NPJ phase diagram using the GEFS Reforecast Version 2 dataset (Hamill et al., 2013). Their analysis found that ensemble mean forecasts verifying during jet retraction and equatorward shift regimes were associated with larger medium-range forecast errors than forecasts verifying during jet extension and poleward

shift regimes. Consideration of the worst-performing 9-day NPJ phase diagram forecasts also found that the worst forecasts occurred in conjunction with rapid NPJ regime transitions towards an equatorward shift regime as well as the development of North Pacific blocking ridges.

A limitation to the Winters et al. (2019a) analysis is that it focuses on one ensemble prediction system and does not consider the extent to which the forecast skill of the NPJ extends into subseasonal time scales. Furthermore, prior work on North American weather regimes does not quantify the forecast skill associated with regime transitions, which are periods that can often lead to substantial downstream impacts over North America (e.g., Bosart et al., 2017). The NPJ phase diagram is well suited for such an analysis, much like those diagrams used by Matsueda & Palmer (2018) and Ferranti et al. (2018) to describe Euro-Atlantic weather regimes, since it allows for observable transitions between regimes and serves as an objective tool to evaluate the ability of models to simulate the cumulative upper-tropospheric flow response to tropical and midlatitude forcing. The remainder of this study is organized as follows. Section 2 discusses the data and methodology used to construct the NPJ phase diagram and NPJ phase diagram forecasts. Section 3 examines the biases and multi-model skill of NPJ phase diagram forecasts. Section 4 considers the evolution of the synoptic-scale flow pattern associated with the best- and worst-performing NPJ phase diagram forecasts from each model, and section 5 provides a discussion of the main conclusions from this work.

## **2. Data and methods**

### *2.1. Data*

This study uses data at 6-h intervals during September–May 1979–2019 from the National Centers for Environmental Prediction (NCEP) Climate Forecast System Reanalysis

(CFSR; Saha et al., 2010, 2014) as well as data during September–May from the Subseasonal-to-Seasonal (S2S) Reforecast Database hosted by the European Centre for Medium-Range Weather Forecasts (ECMWF; Vitart et al., 2017). The CFSR features 0.5° horizontal grid spacing and 64 vertical levels that extend from the surface to 0.26 hPa. The S2S Reforecast Database consists of reforecasts from 11 operational centers, each with a different reforecast period, ensemble size, forecast frequency, forecast length, and model version. Reforecast data are stored on 10 pressure levels and a 1.5° × 1.5° latitude-longitude grid, are initialized at 0000 UTC, and are available at forecast lead times as long as 32–61 days at 24-h intervals. Exceptions to this format are reforecasts from the Australian Bureau of Meteorology (BoM), which are stored on a gaussian grid, and reforecasts from the Japan Meteorological Agency (JMA), which are initialized at 1200 UTC.

To ensure uniformity in the forthcoming analyses, this study does not consider reforecasts from the BoM and JMA, and only uses reforecasts from the nine operational centers identified in Table 1. These centers include Environment and Climate Change Canada (ECCC), Météo-France/Centre National de Recherche Meteorologiques (CNRM), the Institute of Atmospheric Sciences and Climate of the National Research Council (ISAC), the Korea Meteorological Administration (KMA), NCEP, the UK Met Office (UKMO), the Hydrometeorological Center of Russia (HMCR), ECMWF, and the China Meteorological Administration (CMA). The reforecasts from a particular center are constructed using either a “fixed” version of a forecast model or “on the fly” using the current version of a forecast model on the date reforecasts were conducted. For this study, the most recent version of a forecast model prior to 2019 is used to acquire “fixed” reforecast data, and those reforecasts that were conducted during 2019 represent reforecast data that was compiled “on the fly”. Some “on the

fly” reforecasts from the CMA model were also conducted during 2020 to ensure that reforecasts are available throughout September–May during the CMA’s reforecast period. Full details on the characteristics of each reforecast dataset are discussed at length in Vitart et al. (2017).

## 2.2. *The NPJ phase diagram*

The NPJ phase diagram is constructed in an identical manner as in Winters et al. (2019a) with slight modifications to align with the format of the S2S Reforecast Database. Therefore, the forthcoming discussion in this subsection mirrors that from Winters et al. (2019a). First, CFSR data are regridded to 1.5° horizontal grid spacing to match the grid spacing of the reforecast data. Next, 300-hPa zonal wind anomalies from the CFSR are calculated at 6-h intervals during September–May 1979–2019 for each grid point within a North Pacific domain (10.5–79.5°N; 100.5–240°E) that aligns with those used in prior work on NPJ variability (e.g., Jaffe et al., 2011; Griffin & Martin, 2017; Winters et al., 2019a,b). 300-hPa zonal wind anomalies are determined with respect to the CFSR climatology, which is calculated at 6-h intervals for each grid point by retaining the first four harmonics of the mean annual cycle. Note that S2S reforecast data are only available at 300 hPa and 200 hPa. Therefore, the use of 300-hPa zonal wind anomalies in this study represents a departure from the 250-hPa zonal wind anomalies that Winters et al. (2019a) employ in their development of the NPJ phase diagram.

A traditional EOF analysis (Wilks, 2011) is performed on the aforementioned 300-hPa zonal wind anomaly data from the CFSR to reveal the two leading modes of NPJ variability (Figs. 2a,b). EOF 1 explains 9.9% of the variance and corresponds to a zonal extension or retraction of the climatological jet-exit region. EOF 2 explains 7.2% of the variance and corresponds to a poleward or equatorward shift of the climatological jet-exit region. The two leading EOFs, and their explained variance, are similar to those found in prior work (e.g.,



Athanasiadis et al., 2010; Jaffe et al., 2011; Griffin & Martin, 2017; Winters et al., 2019a), and are statistically well separated (North et al., 1982). To instill confidence that the identified NPJ regimes are robust, the same modes of NPJ variability found using 6-h data from the CFSR were also observed when EOF analyses were performed on monthly-averaged zonal wind anomaly data as well as on 6-h data from ERA-Interim (Dee et al., 2011). In particular, the correlation and median absolute difference between the principal component (PC) time series obtained from separate EOF analyses on CFSR and ERA-Interim data were 0.99 and 0.03, respectively.

The temporal evolution of the NPJ with respect to the two leading EOFs is characterized using the PC time series that are returned from the traditional EOF analysis. For this study, 6-h PC data are normalized to unit variance and are averaged over a 5-day period centered on each analysis time. This 5-day average of the PCs removes the high frequency variability of the jet on daily time scales but retains the lower frequency variability of the jet on synoptic time scales. The PCs at a particular analysis time can be visualized by plotting them on the NPJ phase diagram shown in Fig. 2c. The distance along the  $x$ -axis in the NPJ phase diagram identifies how strongly 300-hPa zonal wind anomalies at that time project onto EOF 1, where positive values represent a jet extension and negative values represent a jet retraction. The distance along the  $y$ -axis in the NPJ phase diagram identifies how strongly 300-hPa zonal wind anomalies at that time project onto EOF 2, where positive values represent a poleward shift and negative values represent an equatorward shift. The projection of PCs onto the two leading EOFs over a selected time period produces a trajectory within the NPJ phase diagram that describes the NPJ evolution in the context of the two leading EOFs.

The NPJ phase diagram is subsequently used to classify the state of the NPJ into four NPJ regimes based on whether the magnitude of PC 1 or PC 2 is larger and whether the NPJ resides

at a distance of greater than 1 PC unit from the origin. A projection that falls within a radius of 1 PC unit of the origin of the NPJ phase diagram represents an NPJ that does not project well onto the two leading EOFs or that resembles climatology. For reference, the NPJ typically resides within each of the four primary NPJ regimes approximately 15% of the time and within the unit circle centered on the origin approximately 40% of the time (Winters et al., 2019a). There are generally no preferred transitions between NPJ regimes (i.e., cross correlations between PC 1 and PC 2 are close to zero at all time lags), and the autocorrelation functions for PC 1 and PC 2 drop below 0.5 after 1 week (Fig. 3a), which can serve as a benchmark for the forthcoming analysis in section 3 that evaluates the forecast skill added by each S2S model (e.g., Pegion et al. 2019; Domeisen & Butler, 2020; Feng et al. 2021).

### *2.3. NPJ phase diagram reforecasts and verification*

300-hPa zonal wind anomalies from the nine reforecast datasets identified in Table 1 are used to construct ensembles of NPJ phase diagram forecasts with forecast lead times as long as 32–61 days, depending on the model. To start, 300-hPa zonal wind anomalies are calculated for each ensemble member and at every forecast lead time based on the CFSR climatology. This is done to provide a baseline quantification of forecast skill for each model and to identify any biases in each model’s representation of the NPJ. The zonal wind anomalies associated with each ensemble member forecast are then projected onto the two leading modes of NPJ variability shown in Fig. 2 to construct an ensemble of trajectories within the NPJ phase diagram that describe the forecast evolution of the NPJ (e.g., Fig. 3b). As with the CFSR data, the forecast PCs within a 5-day window centered on each forecast lead time are averaged together to remove high frequency variations of the NPJ on daily time scales. The 5-day average forecast PCs at 0-h, 24-h, and 48-h lead times are specifically calculated by appending CFSR PCs 48-h, 24-h, and 0-h

prior to the start of the forecast period onto the beginning of the forecast PC time series associated with each ensemble member. All ensemble member NPJ phase diagram forecasts initialized at the same time from a particular model are then averaged together to produce an ensemble mean NPJ phase diagram forecast.

NPJ phase diagram forecasts are evaluated by calculating the Euclidean distance between the ensemble mean forecast position of the NPJ within the NPJ phase diagram at a particular forecast lead time and the verifying position of the NPJ at that same forecast lead time using the CFSR. These Euclidean distance statistics are calculated for individual ensemble member NPJ phase diagram forecasts, as well. Note that a reanalysis product must be used for verification given that 0-h forecasts are not available at a daily frequency for each model within the S2S dataset. Forecasts are then classified based on the NPJ regime at the time of forecast initialization as well as the observed NPJ regime at the time of forecast verification using the position of the NPJ within the NPJ phase diagram according to Fig. 2c. This classification of forecasts permits an examination of the extent to which forecast performance varies across models and the four primary NPJ regimes. Forecasts verifying during the month of June are excluded from any calculated forecast statistics given that the NPJ phase diagram is derived solely from zonal wind anomaly data during September–May.

Once these baseline statistics are obtained, the analyses described above are repeated by calculating forecast 300-hPa zonal wind anomalies using each model’s lead-dependent climatology rather than the CFSR climatology. These analyses account for biases in each model’s representation of the NPJ as a function of forecast lead time and allow for a quantification of whether bias correction improves the predictive skill of the NPJ on S2S time scales. Each model’s lead-dependent climatology is constructed by averaging all forecasts at the

same forecast lead time that were initialized within 10 days of a selected calendar day during that model's reforecast period. Similar to Robertson et al. (2020), no cross validation is used in the calculation of model climatologies. EOF analyses performed on the bias-corrected forecast anomalies from each model consistently reproduce the same two leading modes of NPJ variability shown in Figs. 2a,b (not shown).

The present study also identifies the synoptic-scale flow patterns and evolutions that are associated with the best- and worst-performing NPJ phase diagram forecasts from each model. For this purpose, the bias-corrected NPJ forecasts are used. The best- and worst-performing forecasts are identified in a similar manner as Winters et al. (2019a, see their Fig. 10 for a schematic) using both (1) the cumulative ensemble mean Euclidean distance error in the context of the NPJ phase diagram during days 3–21 of the forecast period and (2) the cumulative ensemble member Euclidean distance error during the same period. This forecast period is selected to remove the influence of CFSR PCs on short-lead forecast errors. The best-performing forecasts are those forecasts that rank in the lowest 10% in terms of both the cumulative ensemble mean error and the cumulative ensemble member error for a particular model, whereas the worst-performing forecasts are those forecasts that rank in the highest 10% in terms of both the cumulative ensemble mean error and the cumulative ensemble member error for a particular model. The use of both criteria identifies the best-performing forecasts as those that are accurate and confident (i.e., small ensemble spread). The worst-performing forecasts based on both criteria are those that are inaccurate and uncertain (i.e., large ensemble spread) *or* inaccurate but confident (i.e., small ensemble spread). Put another way, the worst-performing forecasts are those that are the most inaccurate, regardless of the ensemble spread.

### 3. Multi-model performance of NPJ phase diagram forecasts

The total number of valid NPJ phase diagram forecasts from each model (i.e., only those forecasts that are initialized *and* verified during September–May) is shown as a function of forecast lead time in Fig. 4a. Each model is associated with at least 500 valid NPJ phase diagram forecasts at every forecast lead time, with those models that feature a greater forecast frequency (i.e., the NCEP, ISAC, and ECMWF) characterized by larger sample sizes. While each model is initialized at different frequencies and over different years (Table 1), Fig. 4a reveals that there is a suitable sample size of reforecasts from each model from which to draw conclusions concerning the predictability of the NPJ on subseasonal timescales.

First, the analysis considers the baseline skill of NPJ phase diagram forecasts without the application of bias correction. The average ensemble mean distance error of NPJ phase diagram forecasts increases exponentially during week 1 of the forecast period, increases linearly during week 2, and levels off during week 3 for all models. The average ensemble mean error remains approximately constant thereafter, suggesting that any differentiable skill of NPJ phase diagram forecasts diminishes after 21 days (Fig. 4b). The difference in the average ensemble mean error between models at any forecast lead time is also no larger than 0.5 PC units, with the ECMWF model exhibiting the lowest average ensemble mean error at all forecast lead times for which it features a valid forecast. Note that the larger ensembles (e.g., ECMWF, CNRM, HMCR) aren't uniformly associated with lower average ensemble mean errors, as the HMCR model ranks in the top 50% of all models in terms of its average ensemble mean error at every forecast lead time. Figure 4c shows the percent of ensemble member forecasts from each model that correctly identify the verifying NPJ regime at each forecast lead time and reveals that all models are significantly more skillful at identifying the prevailing NPJ regime compared to random chance

at lead times shorter than 21–28 days. The largest difference in performance between forecast models is maximized near the end of week 1 (Fig. 4c), where some models are approximately 20% less accurate at identifying the prevailing NPJ regime than the best-performing model (i.e., ECMWF).

Motivated by the observation that NPJ phase diagram forecasts exhibit skill compared to climatology into weeks 3 and 4 of the forecast period (Figs. 4b,c), the forthcoming analysis considers the extent to which NPJ phase diagram forecast errors vary based on the initial NPJ configuration. Figures 5a,c,e,g show the number of forecasts from each model that are initialized within each of the four primary NPJ regimes as a function of forecast lead time. In contrast to earlier analyses, forecast error (Figs. 5b,d,f,h) is now expressed as a percentage relative to the average ensemble mean error of all forecasts from a particular model that are initialized within one of the four primary NPJ regimes. Forecasts that are initialized within the origin of the NPJ phase diagram are not factored into this analysis since the NPJ does not project strongly onto one of the leading modes of NPJ variability. Positive percentages indicate that ensemble mean forecast errors are larger than average when a model is initialized during a certain NPJ regime, whereas negative percentages indicate that ensemble mean forecast errors are smaller than average.

Figure 5d reveals that forecasts initialized during a jet retraction feature an ensemble mean forecast error that is 10–20% greater than each model’s average at a 7-day lead time, whereas forecasts initialized during a poleward shift feature errors that are 5–15% less than each model’s average at the same lead time (Fig. 5f). Forecasts initialized during a jet extension are characterized by errors that are between 10% less and 5% greater than each model’s average at 0–2-week lead times (Fig. 5b), and forecasts initialized during an equatorward shift are

characterized by errors that are between 5% less and 10% greater than each model's average at 0–2-week lead times. At lead times beyond 2 weeks, the forecast errors associated with each NPJ regime are comparable to one another. Consequently, there does not appear to be a systematic difference in forecast performance based on the initial NPJ regime at lead times longer than 2 weeks as the forecasts are further removed from the influence of the model's initial conditions.

Figure 6 considers the ensemble mean forecast error associated with each model based on the NPJ regime at the time of forecast verification. This approach evaluates the extent to which forecast performance varies based on the character of the NPJ evolution following forecast initialization. The number of forecasts associated with each model as a function of the verifying NPJ regime are shown in Figs. 6a,c,e,g. Overall, NPJ phase diagram forecasts that verify during a jet retraction (Fig. 6d) or equatorward shift (Fig. 6h) exhibit systematically larger ensemble mean forecast errors than forecasts that verify during a jet extension (Fig. 6b) or poleward shift (Fig. 6f) at lead times less than 7 days. This result aligns with that found by Winters et al. (2019a) using the GEFS Reforecast Version 2 dataset and implies that forecasts associated with the development of a North Pacific ridge (Figs. 1c,f) during week 1 feature greater ensemble mean forecast errors across all models.

At lead times longer than 7 days, the performance of NPJ phase diagram forecasts verifying during each NPJ regime is dependent on the model. In particular, the forecasts with the largest errors at lead times exceeding 2 weeks verify during an equatorward shift regime for the ECCC, CNRM, HMCR, ECMWF, and CMA models, during a poleward shift for the KMA and UKMO models, during a jet retraction for the NCEP model, and during a jet extension for the ISAC model (cf. Figs. 6b,d,f,h). Similar variability across models is also observed when considering the verifying NPJ regimes that exhibit the lowest forecast errors at lead times

exceeding 2 weeks. Since the preceding analysis does not yet account for forecast model biases, the observed differences in forecast model performance based on the verifying NPJ regime at lead times exceeding 2 weeks may be related to frequency biases in the prediction of each NPJ regime.

To this aim, Figures 7a–d depict the percent frequency that each NPJ regime is overforecast or underforecast in each model with respect to verification. Note that the ISAC model is not included in this initial analysis and will be discussed separately. For this analysis, each ensemble member initialized using a particular model is treated as a separate forecast of the NPJ regime. Figure 7a reveals that the NCEP model overforecasts the occurrence of jet extensions by approximately 30–40% compared to verification at lead times exceeding 2 weeks, whereas jet extensions are underforecast by all other models by as much as 20%. Conversely, all models overforecast the occurrence of jet retractions by as much as 30% at lead times exceeding 2 weeks, except for the NCEP model, which underforecasts the occurrence of jet retractions by approximately 30% (Fig. 7b).

The frequency of poleward shift and equatorward shift forecasts compared to verification is more variable across models compared to jet extension and jet retraction forecasts. In particular, the HMCR, ECCC, and CNRM models overforecast the occurrence of poleward shifts at lead times exceeding 2 weeks, with an overforecast of poleward shifts by as much as 70–90% during week 4 in the HMCR model (Fig. 7c). Poleward shifts are underforecast by the CMA, ECMWF, NCEP, KMA, and UKMO models by as much as 30% compared to verification at lead times exceeding 2 weeks. Last, equatorward shifts are overforecast by 10–50% in the NCEP, CMA, UKMO, and KMA models, while the ECCC and HMCR models underforecast the occurrence of equatorward shifts by 20–60% (Fig. 7d). Notably, the frequency of CNRM and



ECMWF forecasts of equatorward shifts is comparable to verification throughout the forecast period. The ISAC model is a particularly interesting case (Fig. 7e), in which jet extensions are underforecast by close to 80% during weeks 2–4, and jet retractions are overforecast by 140–200%.

Biases in the forecast frequency of each NPJ regime in Fig. 7 are associated with the forecast errors identified in Fig. 6. Namely, the largest ensemble mean forecast errors during weeks 2–4 in the ECCC, HMCRC, KMA, UKMO, CFSR, and ISAC models are associated with the same verifying NPJ regime for which those models exhibit a low forecast frequency bias (cf. Figs. 6–7). As suggested by Ferranti et al. (2015), this observation implies that the reduced performance of model forecasts that verify in those respective NPJ regimes may be due to the misrepresentation of physical processes that lead to the development of those NPJ regimes. For the ECMWF, CNRM, and CMA models, which feature their largest forecast errors during periods that verify during an equatorward shift, there is not a clear low forecast frequency bias for equatorward shifts. In fact, the CMA exhibits a high forecast frequency bias for equatorward shifts compared to verification. This result implies that these three models are able to represent the physical processes that lead to the development of equatorward shifts with fidelity, but that equatorward shifts may be characterized by low intrinsic predictability.

The same analyses described above are repeated with bias-corrected NPJ phase diagram forecasts that utilize 300-hPa zonal wind anomalies based on each model’s lead-dependent climatology rather than the CFSR. The use of bias-corrected forecasts substantially reduces the regime frequency biases shown in Fig. 7. While not shown explicitly, all bias-corrected forecast statistics are similar to those shown in Fig. 3 and feature slightly reduced ensemble mean errors at lead times exceeding 2 weeks. Additionally, the classification of bias-corrected forecast errors

based on the NPJ regime at the time of forecast initialization is similar to the results shown in Fig. 5 (not shown). Substantial differences are noted in comparison to the baseline forecasts, however, when classifying bias-corrected forecast errors based on the verifying NPJ regime (cf., Figs. 6 and 8). Namely, bias-corrected forecast errors (Fig. 8) are not as substantial as those shown in Fig. 6, and there is a general agreement between model errors associated with each verifying NPJ regime at all forecast lead times. In particular, forecasts verifying during jet retractions and equatorward shifts typically exhibit larger than normal forecast errors, whereas forecasts verifying during jet extensions and poleward shifts typically exhibit reduced forecast errors compared to each model's climatology. The general agreement among bias-corrected model errors for each verifying NPJ regime suggests that NPJ evolutions towards a jet retraction or equatorward shift may be characterized by a lower degree of intrinsic predictability than NPJ evolutions towards a jet extension or poleward shift.

Reliability diagrams that evaluate the probabilistic detection of the verifying NPJ regime for the three largest ensembles (i.e., CNRM, ECMWF, HMCR) further demonstrate that bias-corrected NPJ phase diagram forecasts are underdispersive at forecast lead times exceeding 7 days (Fig. 9). Consequently, ensemble forecasts from these three models tend to be overconfident in the development of a particular NPJ regime at medium-range and subseasonal lead times. In particular, both CNRM (Fig. 9a) and ECMWF (Fig. 9b) forecast probabilities exceeding 50% are overconfident by 5–20% at forecast lead times exceeding 14 days, whereas HMCR forecast probabilities exceeding 50% are overconfident by 20–40% (Fig. 9c). The reduced performance of HMCR forecasts compared to CNRM and ECMWF forecasts is also apparent in Fig. 9d, which reveals that the Brier Skill Score (Wilks 2011) for HMCR forecasts is less than that for the CNRM and ECMWF models at all forecast lead times.

#### 4. Synoptic-scale flow patterns associated with the best- and worst-performing forecasts

Results from the previous section suggest that the best- and worst-performing subseasonal NPJ phase diagram forecasts are associated with different NPJ regimes (e.g., Figs. 5 and 8). Consequently, the forthcoming analysis considers the synoptic-scale characteristics of the 21-day period following the initiation of a best- and worst-performing forecast from each model. As mentioned in section 2.3, the best-performing forecasts are those bias-corrected forecasts in which there is both a low cumulative ensemble mean distance error in the context of the NPJ phase diagram (i.e., an accurate forecast) and a low cumulative ensemble member distance error (i.e., a confident forecast) during days 3–21 of the forecast period. The worst-performing forecasts are those in which there is both a high cumulative ensemble mean distance error in the context of the NPJ phase diagram and a high cumulative ensemble member distance error (i.e., the most inaccurate forecasts).

The average position of the NPJ within the NPJ phase diagram on the date a best-performing forecast is initialized from each forecast model is shown in Fig. 10a and reveals that the NPJ is generally displaced towards a poleward shift regime. The models are clustered near the origin, however, which suggests that the NPJ may also be close to its climatological state or exhibit considerable variability in its state at the time a best-performing forecast is initialized. The state of the NPJ at the start of a worst-performing forecast period is displaced towards a jet retraction or equatorward shift (Fig. 10b). This result aligns well with Figs. 5d,h, which indicate that forecast errors are often higher than each model's average during the first 2 weeks of the forecast period when a model is initialized during those two NPJ regimes.

Figures 10c,d illustrate the composite evolution of the NPJ during the 21-day period following the initialization of a best- and worst-performing forecast from each model. The composite evolution of the NPJ associated with each model is calculated by projecting 300-hPa zonal wind anomalies from the CFSR onto the NPJ phase diagram during the 21-day period following the initialization of each best- or worst-performing forecast, resulting in a series of trajectories within the NPJ phase diagram. These trajectories are then shifted so that they all begin at the origin of the NPJ phase diagram and the PCs corresponding to the same day after forecast initialization are averaged together to construct a composite trajectory. Note that the trajectories shown in Figs. 10c,d do not show forecast trajectories, but instead depict the how the NPJ evolved in reality following a best- or worst-performing forecast.

The composite CFSR trajectories during the 21-day period following a best-performing forecast from each model are clustered near the origin and exhibit a slight transition towards a jet extension or poleward shift during the first few days of the forecast period (Fig. 10c). The 21-day period following a worst-performing forecast, on the other hand, exhibits an opposite character (Fig. 10d). Namely, the worst-performing forecast periods generally feature an NPJ that evolves towards an equatorward shift or a jet retraction during the first half of the forecast period before returning towards the origin. Given that the NPJ is already displaced towards a jet retraction or equatorward shift at the time a worst-performing forecast is initialized (Fig. 10b), the NPJ trajectories shown in Fig. 10d indicate that the NPJ amplifies its projection onto these two NPJ regimes during the subsequent 21-day period.

Figure 10e shows a composite of the ensemble mean NPJ phase diagram forecast trajectory associated with a worst-performing forecast from each model. Overall, each model's forecast trajectory exhibits errors in the forecasted NPJ regime transition and/or in the amplitude

of a particular NPJ regime (cf., Figs. 10d,e). Furthermore, the forecast trajectories (Fig. 10e) are more biased towards a jet extension and poleward shift at the end of the 21-day forecast period than observations (Fig. 10d), which suggests the models may be too quick to transition the jet out of a jet retraction or equatorward shift regime. Given that both jet retractions and equatorward shifts feature upper-tropospheric ridging over the North Pacific (Figs. 1c,g), these differences between the forecast and observed trajectories indicate that forecast errors may be related to each model's representation of physical processes that govern the extent and duration of North Pacific flow amplification. These physical processes can include the magnitude of diabatic heating and upper-level irrotational outflow associated with midlatitude cyclogenesis events along the North Pacific storm track (e.g., Torn & Hakim 2015; Teubler & Riemer 2016; Martinez-Alvarado et al., 2016; Bosart et al., 2017).

The synoptic-scale flow patterns associated with the worst-performing forecasts from each model are examined further by compositing CFSR mass and wind fields 0 days (Fig. 11), 10 days (Fig. 12), and 20 days (Fig. 13) following the initialization of a worst-performing forecast. At the time of forecast initialization, every model features some degree of anomalous upper-tropospheric ridging over the central North Pacific (Fig. 11). For some models, such as the ECCC, CNRM, KMA, UKMO, ECMWF, and CMA (Figs. 11a,b,d,f,h,i), the North Pacific ridge is more anomalous, suggesting that the worst-performing forecasts for those models may be preferentially initialized during or immediately following ridge amplification rather than prior to ridge amplification. Ten days after forecast initialization, the synoptic-scale flow pattern features a well-developed upper-tropospheric ridge across the high-latitude North Pacific within each model (Fig. 12). The presence of a high-latitude ridge is consistent with both a jet retraction and equatorward shift regime (Figs. 1c,g), which are the same NPJ regimes that are generally

characterized by the greatest forecast errors at the time of forecast verification during the week 1–2 forecast period (Figs. 8b,d).

Twenty days after the initialization of a worst-performing forecast, the composite upper-tropospheric flow patterns feature considerable differences across models (Fig. 13). In particular, the ECCC, CNRM, NCEP, UKMO, ECMWF, and CMA models (Figs. 13a,b,e,f,h,i) continue to feature an amplified upper-tropospheric ridge over the North Pacific, albeit slightly farther west than observed in Fig. 12 in some cases. Conversely, the composite flow patterns following the worst-performing forecasts from the ISAC, KMA, and HMCR models (Figs. 13c,d,g) indicate that the upper-tropospheric ridge over the central North Pacific decays more rapidly than in the other models 20 days after forecast initialization. All models also exhibit considerable differences with respect to the character of the resultant flow pattern over North America. To synthesize the composite evolutions shown in Figs. 11–13, the largest NPJ phase diagram forecast errors from each model are clearly associated with North Pacific ridge amplification during the week 1–2 period. After that, the variable synoptic-scale flow patterns that prevail 20 days after forecast initialization imply that aspects of the life cycle of North Pacific ridges, such as their persistence, retrogression, and decay, may hinder model performance.

Last, Winters et al. (2019b, their Fig. 13) demonstrate that periods in which the NPJ evolves towards an equatorward shift (similar to those trajectories shown in Fig. 10d) increase the likelihood of extreme cold events across the continental U.S. Indeed, the composite upper-tropospheric flow pattern 10 days after a worst-performing forecast from each model features an anomalous trough over central Canada (Fig. 12). The longitudinal juxtaposition of a high-latitude ridge over the North Pacific and trough over central Canada subsequently favors the development of an anomalous surface anticyclone across Alaska and western Canada in the

aforementioned composites (Fig. 14). To the east of this anticyclone, perturbation northerly geostrophic flow is conducive to the equatorward transport of anomalously cold air towards southern Canada and the northern U.S. Therefore, the composite lower-tropospheric temperature patterns following a worst-performing forecast suggest that the worst-performing forecasts may coincide with the occurrence of North American cold-air outbreaks during the week 2 period, potentially limiting the prediction of those events.

## **5. Conclusions**

This study examines the subseasonal predictability of the state and evolution of the NPJ across nine models within the S2S Reforecast Database hosted by ECMWF (Vitart et al., 2017). The state and evolution of the NPJ is specifically examined in the context of an NPJ phase diagram (Winters et al., 2019a), which identifies periods during which the NPJ is characterized by an extended or retracted state, and during which the NPJ is poleward or equatorward shifted relative to its climatological position. 300-hPa zonal wind anomaly data from the S2S Reforecast Database are then projected onto the NPJ phase diagram to construct ensemble forecasts describing the state and evolution of the NPJ at subseasonal time scales. NPJ phase diagram forecasts are evaluated by considering the Euclidean distance between the forecast position of the NPJ within the NPJ phase diagram at a particular lead time and the verification position of the NPJ in the CFSR. Forecasts are also partitioned based on whether a forecast is initialized or verified during a particular NPJ regime to determine the extent to which verification statistics vary depending on those metrics. Last, the best- and worst-performing forecasts associated with each model are identified to examine the synoptic-scale flow evolution that characterizes the 21-day period following a best- or worst-performing forecast from each model.

An evaluation of NPJ phase diagram forecasts reveals that skillful predictions of the state and evolution of the NPJ can extend into the week 3 forecast period, with the ECMWF model featuring the lowest forecast errors among all models at every forecast lead time. The fact that the skill of NPJ phase diagram forecasts extends into the week 3 period is consistent with prior work on North American weather regimes, which suggest that skillful predictions are generally possible at lead times of 15 days (e.g., Vigaud et al., 2018; Robertson et al., 2020). NPJ phase diagram forecasts of the verifying NPJ regime from the three largest ensembles considered as part of this study (i.e., ECMWF, CNRM, HMCR) are also generally reliable at forecast lead times extending into weeks 2–3, but are uniformly underdispersive, and thus overconfident in the development of a particular NPJ regime.

Forecast errors in the context of the NPJ phase diagram vary depending on the NPJ regime at the time of forecast initialization during the first two weeks of the forecast period. Thereafter, forecast errors do not show much dependence on the initial NPJ regime as the model forecast is further removed from knowledge of atmospheric initial conditions. Overall, forecasts initialized during a jet retraction feature 7-day forecast errors that are 10–20% larger than all forecasts that are initialized during one of the four primary NPJ regimes, whereas forecasts initialized during a poleward shift feature forecast errors that are 5–15% smaller. Forecasts verifying during jet retractions and equatorward shifts also exhibit larger errors during the first two weeks of the forecast period compared to forecasts verifying during jet extensions and poleward shifts. Notably, both jet retractions and equatorward shifts are associated with the development of an upper-tropospheric North Pacific ridge, which can be strongly influenced by diabatic processes that occur within midlatitude cyclones along the Pacific storm track or in conjunction with tropical convection (e.g., Torn & Hakim, 2015; Teubler & Riemer, 2016;



Martinez-Alvarado et al., 2016; Bosart et al., 2017; Breeden et al., 2020). The inability for models to represent the extent, magnitude, and cumulative influence of these diabatic processes on the upper-tropospheric flow pattern is hypothesized to contribute to the larger-than-average forecast errors associated with jet retractions and equatorward shifts during the first two weeks of the forecast period.

At lead times longer than two weeks, forecast errors associated with each NPJ regime appear to be strongly influenced by biases in each model's representation of the jet at subseasonal lead times. Namely, NPJ regimes that were characterized by a low forecast frequency bias at subseasonal lead times within a particular model were often the same NPJ regimes that were associated with the largest forecast errors at the time of verification for that model. The use of bias-corrected forecasts resolved these forecast frequency biases and resulted in stronger agreement between forecast model errors at subseasonal lead times. Namely, forecasts verifying during jet retractions or equatorward shifts were generally associated with the largest forecast errors at subseasonal lead times. These results indicate that bias-corrected NPJ phase diagram forecasts have the potential to identify periods that may exhibit enhanced skill compared to each model's climatology at subseasonal lead times based on the anticipated NPJ evolution.

The best-performing forecasts associated with each model occurred during periods in which the NPJ featured a slight poleward shift, whereas the worst-performing forecasts featured an NPJ that evolved towards a jet retraction or equatorward shift. Composites of the 21-day period following the initiation of a worst-performing forecast from each model indicated that the largest NPJ forecast errors coincided with the development of an upper-tropospheric North Pacific ridge during the first 10 days after forecast initialization and the subsequent maintenance,

retrogression, or decay of that ridge over the next 10 days. This result generalizes the analysis from Winters et al. (2019a), who found a similar flow pattern was associated with the worst-performing forecasts on medium-range time scales in the GEFS Reforecast Version 2 dataset, and reaffirms that the life cycle of upper-tropospheric blocks remains a considerable predictability challenge at subseasonal lead times (e.g., D’Andrea et al., 1998; Pelly & Hoskins, 2003; Ferranti et al., 2015; Matsueda & Palmer, 2018).

The results from this study motivate new avenues for future work. First, differences in the forecast frequency of NPJ regimes at lead times exceeding two weeks within the baseline forecasts from each model motivate further investigation into each model’s representation of physical processes that lead to the development of each NPJ regime (i.e., diabatic heating from midlatitude and tropical sources and its subsequent influence on the character of the upper-tropospheric flow pattern). Second, the present results do not consider the extent to which forecast errors associated with each NPJ regime translate to forecast errors over the North American continent. Therefore, a study that considers the relationship between the prevailing NPJ regime and downstream forecast errors would be a worthwhile endeavor. Finally, North American weather is also influenced by the state and evolution of the synoptic-scale flow pattern over the North Atlantic. A similar approach as used in this study can be applied to the North Atlantic jet to examine the ability of models to accurately capture the state and evolution of that jet.

## **Acknowledgments**

The author is grateful to personnel at the NCEP Weather Prediction Center and Climate Prediction Center, whose constructive comments and feedback informed various stages of this

work. The author is also appreciative to the Editor and two anonymous reviewers, whose constructive comments greatly improved the manuscript. Support for the author to perform this work was provided by start-up funding furnished by the University of Colorado Boulder.

#### **Data Availability Statement**

CFSR data utilized for this study is publicly available from the NCAR Research Data Archive (<https://doi.org/10.5065/D69K487J>). This work is based on S2S Reforecast data available from ECMWF. S2S is a joint initiative of the World Weather Research Programme (WWRP) and the World Climate Research Programme (WCRP). The original S2S database is hosted at ECMWF as an extension of the TIGGE database (Vitart et al., 2017). A database of NPJ phase diagram forecasts derived from the S2S Reforecast Database is archived at the University of Colorado Boulder (Winters, 2021; <https://scholar.colorado.edu/concern/datasets/0v838153k>) Any computer programs necessary to reproduce the results shown in this study are available from the author upon request.

## References

- Amini, S., & Straus, D. M. (2019). Control of storminess over the Pacific and North America by circulation regimes. *Climate Dynamics*, 52, 4749–4770. <https://doi.org/10.1007/s00382-018-4409-7>.
- Archambault, H. M., Keyser, D., Bosart, L. F., Davis, C. A., & Cordeira, J. M. (2015). A composite perspective of the extratropical flow response to recurving western North Pacific tropical cyclones. *Monthly Weather Review*, 143, 1122–1141. <https://doi.org/10.1175/MWR-D-14-00270.1>.
- Athanasiadis, P. J., Wallace, J. M., & Wettstein, J. J. (2010). Patterns of wintertime jet stream variability and their relation to the storm tracks. *Journal of the Atmospheric Sciences*, 67, 1361–1381. <https://doi.org/10.1175/2009JAS3270.1>.
- Bosart, L. F., Moore, B. J., Cordeira, J. M., & Archambault, H. M. (2017). Interactions of North Pacific tropical, midlatitude, and polar disturbances resulting in linked extreme weather events over North America in October 2007. *Monthly Weather Review*, 145, 1245–1273. <https://doi.org/10.1175/MWR-D-16-0230.1>.
- Breeden, M.L., Hoover, B. T., Newman, M., & Vimont, D. J. (2020). Optimal North Pacific blocking precursors and their deterministic subseasonal evolution during boreal winter. *Monthly Weather Review*, 148, 739–761. <https://doi.org/10.1175/MWR-D-19-0273.1>.
- Cassou, C. (2008). Intraseasonal interaction between the Madden–Julian Oscillation and the North Atlantic Oscillation. *Nature*, 455, 523–527. <https://doi.org/10.1038/nature07286>.
- Cordeira, J. M., & Bosart, L. F. (2010). The antecedent large-scale conditions of the “Perfect Storms” of late October and early November 1991. *Monthly Weather Review*, 138, 2546–2569. <https://doi.org/10.1175/2010MWR3280.1>.

683 Corti, S., Molteni, F. & Palmer, T. N. (1999). Signature of recent climate change in frequencies  
684 of natural atmospheric circulations. *Nature*, 398, 799–802. <https://doi.org/10.1038/19745>.

685 D’Andrea, F., Tibaldi, S., Blackburn, M., Boer, G., Déqué, M., Dix, M. R. (1998). Northern  
686 Hemisphere atmospheric blocking as simulated by 15 atmospheric general circulation  
687 models in the period 1979–1988. *Climate Dynamics*, 14, 385–407.  
688 <https://doi.org/10.1007/s003820050230>.

689 Dawson, A., & Palmer, T. N. (2014). Simulating weather regimes: Impact of model resolution  
690 and stochastic parameterization. *Climate Dynamics*, 44, 2177–2193.  
691 <https://doi.org/10.1007/s00382-014-2238-x>.

692 Dee, D. P., Uppala, S. M., Simmons, A. J., Berrisford, P., Poli, P., Kobayashi, S., et al., (2011).  
693 The ERA-Interim reanalysis: Configuration and performance of the data assimilation  
694 system. *Quarterly Journal of the Royal Meteorological Society*, 137, 553–597.  
695 <http://doi.org/10.1002/qj.828>.

696 Domeisen, D. I. V. & Butler, A. H., (2020). Stratospheric drivers of extreme events at the Earth’s  
697 surface. *Communications Earth & Environment*, 1, 59, [http://doi.org/10.1038/s43247-](http://doi.org/10.1038/s43247-020-00060-z)  
698 [020-00060-z](http://doi.org/10.1038/s43247-020-00060-z).

699 Feng, P.-N., Lin, H., Derome, J., & Merlis, T. M. (2021). Forecast skill of the NAO in the  
700 subseasonal-to-seasonal prediction models. *Journal of Climate*, 34, 4757–4769.  
701 <https://doi.org/10.1175/JCLI-D-20-0430.1>.

702 Ferranti, L., Corti, S., & Janousek, M. (2015). Flow-dependent verification of the ECMWF  
703 ensemble over the Euro-Atlantic sector. *Quarterly Journal of the Royal Meteorological*  
704 *Society*, 141, 916–924. <https://doi.org/10.1002/qj.2411>.

705 Ferranti, L., Magnusson, L., Vitart, F., & Richardson, D. S. (2018). How far in advance can we  
 706 predict changes in large-scale flow leading to severe cold conditions over Europe?  
 707 *Quarterly Journal of the Royal Meteorological Society*, 144, 1788–1802.  
 708 <https://doi.org/10.1002/qj.3341>.

709 Grams, C. M., Beerli, R., Pfenninger, S., Staffell, I., & Wernli, H. (2017). Balancing Europe’s  
 710 wind-power output through spatial deployment informed by weather regimes. *Nature*  
 711 *Climate Change*, 7, 557–562. <https://doi.org/10.1038/nclimate3338>.

712 Griffin, K. S., & Martin, J. E. (2017). Synoptic features associated with temporally coherent  
 713 modes of variability of the North Pacific jet stream. *Journal of Climate*, 30, 39–54.  
 714 <https://doi.org/10.1175/JCLI-D-15-0833.1>.

715 Hamill, T. M., Bates, G. T., Whitaker, J. S., Murray, D. R., Fiorino, M., Galarneau Jr., T. J., Zhu,  
 716 Y., & Lapenta, W. (2013). NOAA’s second-generation global medium-range ensemble  
 717 reforecast dataset. *Bulletin of the American Meteorological Society*, 94, 1553–1565.  
 718 <https://doi.org/10.1175/BAMS-D-12-00014.1>.

719 Jaffe, S. C., Martin, J. E., Vimont, D. J., & Lorenz, D. J. (2011). A synoptic climatology of  
 720 episodic, subseasonal retractions of the Pacific jet. *Journal of Climate*, 24, 2846–2860.  
 721 <https://doi.org/10.1175/2010JCLI3995.1>.

722 Jung, T., Vitart F., Ferranti, L., & Morcrette, J.-J. (2011). Origin and predictability of the  
 723 extreme negative NAO winter of 2009/10. *Geophysical Research Letters*, 38, L07701.  
 724 <https://doi.org/10.1029/2011GL046786>.

725 Kimoto, M., & Ghil, M. (1993). Multiple flow regimes in the Northern Hemisphere winter. Part  
 726 I: Methodology and hemispheric regimes. *Journal of the Atmospheric Sciences*, 50,  
 727 2625–2644. [https://doi.org/10.1175/1520-0469\(1993\)050<2625:MFRITN>2.0.CO;2](https://doi.org/10.1175/1520-0469(1993)050<2625:MFRITN>2.0.CO;2).

728 Lee., S. H., Furtado, J. C., & Charlton-Perez, A. J. (2019). Wintertime North American weather  
 729 regimes and the Arctic stratospheric polar vortex. *Geophysical Research Letters*, 46,  
 730 14892–14900. <https://doi.org/10.1029/2019GL085592>.  
 731 Martínez-Alvarado, O., Gray, S. L., & Methven, J. (2016). Diabatic processes and the evolution  
 732 of two contrasting summer extratropical cyclones. *Monthly Weather Review*, 144, 3251–  
 733 3276. <https://doi.org/10.1175/MWR-D-15-0395.1>.  
 734 Matsueda, M., & Kyouda, M. (2016). Wintertime east Asian flow patterns and their  
 735 predictability on medium-range timescales. *Scientific Online Letters on the Atmosphere*,  
 736 12, 121–126. <https://doi.org/10.2151/sola.2016-027>.  
 737 Matsueda, M., & Palmer, T. N. (2018). Estimates of flow-dependent predictability of wintertime  
 738 Euro-Atlantic weather regimes in medium-range forecasts. *Quarterly Journal of the*  
 739 *Royal Meteorological Society*, 144, 1012–1027. <https://doi.org/10.1002/qj.3265>.  
 740 Meehl, G. A., Richter, J. H., Teng, H., Capotondi, A., Cobb, K., Doblas-Reyes, F., et al.  
 741 (2021). Initialized earth system prediction from subseasonal to decadal timescales.  
 742 *Nature Reviews Earth & Environment*, 2, 340–357. [https://doi.org/10.1038/s43017-021-](https://doi.org/10.1038/s43017-021-00155-x)  
 743 00155-x.  
 744 Michelangeli, P.-A., Vautard, R., & Legras, B. (1995). Weather regimes: Recurrence and quasi  
 745 stationarity. *Journal of the Atmospheric Sciences*, 52, 1237–1256.  
 746 [https://doi.org/10.1175/1520-0469\(1995\)052<1237:WRRAS>2.0.CO;2](https://doi.org/10.1175/1520-0469(1995)052<1237:WRRAS>2.0.CO;2).  
 747 Mo, K., & Ghil, M. (1988). Cluster analysis of multiple planetary flow regimes. *Journal of*  
 748 *Geophysical Research: Atmospheres*, 93, 10927–10952.  
 749 <https://doi.org/10.1029/JD093iD09p10927>.

750 National Academies of Sciences, Engineering, and Medicine [NAS]. (2018). *Thriving on Our*  
751 *Changing Planet: A Decadal Strategy for Earth Observation from Space*. Washington,  
752 DC: National Academies Press. <https://doi.org/10.17226/24938>.

753 National Research Council [NRC]. (2010). *Assessment of Intraseasonal to Interannual Climate*  
754 *Prediction and Predictability*. Washington, DC: National Academies Press.  
755 <https://doi.org/10.17226/12878>.

756 North, G. R., Bell, T. L., Cahalan, R. F., & Moeng, F. J. (1982). Sampling errors in the  
757 estimation of empirical orthogonal functions. *Monthly Weather Review*, 110, 699–706.  
758 [https://doi.org/10.1175/1520-0493\(1982\)110<0699:SEITEO>2.0.CO;2](https://doi.org/10.1175/1520-0493(1982)110<0699:SEITEO>2.0.CO;2).

759 Pegion, K., Kirtman, B. P., Becker, E., Collins, D. C., LaJoie, E., Burgman, R., et al. (2019). The  
760 subseasonal experiment (SubX): A multimodel subseasonal prediction experiment.  
761 *Bulletin of the American Meteorological Society*, 100, 2043–2060.  
762 <https://doi.org/10.1175/BAMS-D-18-0270.1>.

763 Pelly, J. L., & Hoskins, B. J. (2003). How well does the ECMWF Ensemble Prediction System  
764 predict blocking? *Quarterly Journal of the Royal Meteorological Society*, 129, 1683–  
765 1702. <https://doi.org/10.1256/qj.01.173>.

766 Quandt, L.-A., Keller, J. H., Martius, O., Pinto, J. G., & Jones, S. C. (2019). Ensemble sensitivity  
767 analysis of the blocking system over Russia in summer 2010. *Monthly Weather Review*,  
768 147, 657–675. <https://doi.org/10.1175/MWR-D-18-0252.1>.

769 Reinhold, B., & Pierrehumbert, R. (1982). Dynamics of weather regimes: Quasi-stationary  
770 waves and blocking. *Monthly Weather Review*, 110, 1105–1145.  
771 [https://doi.org/10.1175/1520-0493\(1982\)110,1105:DOWRQS.2.0.CO;2](https://doi.org/10.1175/1520-0493(1982)110,1105:DOWRQS.2.0.CO;2).



772 Riddle, E. E., Stoner, M., Johnson, N., L'Heureux, M. (2013). The impact of the MJO on clusters  
773 of wintertime circulation anomalies over the North American region. *Climate Dynamics*,  
774 40, 1749–1766. <https://doi.org/10.1007/s00382-012-1493-y>.

775 Robertson, A. W., & Ghil, M. (1999). Large-scale weather regimes and local climate over the  
776 western United States. *Journal of Climate*, 12, 1796–1813. [https://doi.org/10.1175/1520-0442\(1999\)012<1796:LSWRAL>2.0.CO;2](https://doi.org/10.1175/1520-0442(1999)012<1796:LSWRAL>2.0.CO;2).

778 Robertson, A. W., Vigaud, N., Yuan, J., & Tippett, M. K. (2020). Toward identifying  
779 subseasonal forecasts of opportunity using North American weather regimes. *Monthly*  
780 *Weather Review*, 148, 1861–1875. <https://doi.org/10.1175/MWR-D-19-0285.1>.

781 Saha, S., Moorthi, S., Pan, H.-L., Wu, X., Wang, J., Nadiga, S., et al. (2010). The NCEP Climate  
782 Forecast System Reanalysis. *Bulletin of the American Meteorological Society*, 91, 1015–  
783 1057. <https://doi.org/10.1175/2010BAMS3001.1>.

784 Saha, S., Moorthi, S., Wu, X., Wang, J., Nadiga, S., Tripp, P., et al. (2014). The NCEP Climate  
785 Forecast System version 2. *Journal of Climate*, 27, 2185–2208.  
786 <https://doi.org/10.1175/JCLI-D-12-00823.1>.

787 Straus, D. M., Corti, S., & Molteni, F. (2007). Circulation regimes: Chaotic variability versus  
788 SST-forced predictability. *Journal of Climate*, 20, 2251–2272.  
789 <https://doi.org/10.1175/JCLI4070.1>.

790 Straus, D. M., Molteni, F., & Corti, S. (2017). Atmospheric regimes: The link between weather  
791 and the large-scale circulation. In C. L. E. Franzke and T. J. O’Kane (Eds.), *Nonlinear*  
792 *and Stochastic Climate Dynamics* (pp. 105–135). Cambridge, UK: Cambridge University  
793 Press.

794 Teubler, F., & Riemer, M. (2016). Dynamics of Rossby wave packets in a quantitative potential  
795 vorticity–potential temperature framework. *Journal of the Atmospheric Sciences*, 73,  
796 1063–1081. <https://doi.org/10.1175/JAS-D-15-0162.1>.

797 Torn, R. D., & Hakim, G. J. (2015). Comparison of wave packets associated with extratropical  
798 transition and winter cyclones. *Monthly Weather Review*, 143, 1782–1803.  
799 <https://doi.org/10.1175/MWR-D-14-00006.1>.

800 Turasky, E. (2019). *An examination of North Pacific jet regimes conducive to landfalling*  
801 *atmospheric rivers along the west coast of North America* (M.S. Thesis). Retrieved from  
802 ProQuest Dissertations and Theses  
803 ([https://search.proquest.com/docview/2283452686/BFB9D80CD67A438EPQ/2?accounti](https://search.proquest.com/docview/2283452686/BFB9D80CD67A438EPQ/2?accountid=14503)  
804 [d=14503](https://search.proquest.com/docview/2283452686/BFB9D80CD67A438EPQ/2?accountid=14503)). Albany, NY: University at Albany, SUNY.

805 Vautard, R. (1990). Multiple weather regimes over the North Atlantic: Analysis of precursors  
806 and successors. *Monthly Weather Review*, 118, 2056–2081. [https://doi.org/10.1175/1520-](https://doi.org/10.1175/1520-0493(1990)118<2056:MWROTN>2.0.CO;2)  
807 [0493\(1990\)118<2056:MWROTN>2.0.CO;2](https://doi.org/10.1175/1520-0493(1990)118<2056:MWROTN>2.0.CO;2).

808 Vigaud, N., Robertson, A. W., & Tippett, M. K. (2018). Predictability of recurrent weather  
809 regimes over North America during winter from submonthly reforecasts. *Monthly*  
810 *Weather Review*, 146, 2559–2577. <https://doi.org/10.1175/MWR-D18-0058.1>.

811 Vitart, F., Ardilouze, C., Bonet, A., Brookshaw, A., Chen, M., Codorean, C., et al. (2017). The  
812 subseasonal to seasonal (S2S) prediction project database. *Bulletin of the American*  
813 *Meteorological Society*, 98, 163–173. <https://doi.org/10.1175/BAMS-D-16-0017.1>.

814 White, C. J., Carlsen, H., Robertson, A. W., Klein, R. J. T., Lazo, J. K., Kumar, A., et al. (2017).  
815 Potential applications of subseasonal-to-seasonal (S2S) predictions. *Meteorological*  
816 *Applications*, 24, 315–325. <https://doi.org/10.1002/met.1654>.

817 Wilks, D. S. (2011). *Statistical Methods in the Atmospheric Sciences* (3rd ed). Amsterdam,  
818 Netherlands: Elsevier.

819 Winters, A. C., Keyser, D., & Bosart, L. F. (2019a) The development of the North Pacific Jet  
820 Phase Diagram as an objective tool to monitor the state and forecast skill of the upper-  
821 tropospheric flow pattern. *Weather and Forecasting*, 34, 199–219.  
822 <https://doi.org/10.1175/WAF-D-18-0106.1>.

823 Winters, A. C., Bosart, L. F., & Keyser, D. (2019b) Antecedent North Pacific jet regimes  
824 conducive to the development of continental U.S. extreme temperature events during the  
825 cool season. *Weather and Forecasting*, 34, 393–414. [https://doi.org/10.1175/WAF-D-18-](https://doi.org/10.1175/WAF-D-18-0168.1)  
826 [0168.1](https://doi.org/10.1175/WAF-D-18-0168.1).

827 Winters, A. C. (2021) Subseasonal forecasts of the state and evolution of the North Pacific jet  
828 stream [Data set]. University of Colorado Boulder.  
829 <https://scholar.colorado.edu/concern/datasets/0v838153k>  
830

831 **Tables**

<b>Model</b>	<b>Horizontal Resolution</b>	<b>Reforecast Type</b>	<b>Model Version</b>	<b>Reforecast Period</b>	<b>Reforecast Frequency</b>	<b>Forecast Length</b>	<b>Ensemble Members</b>
<b>ECCC</b>	1.5°×1.5°	On the fly	2019	1998–2017	Every 7 days	32 days	4
<b>CNRM</b>	1.5°×1.5°	Fixed	12/01/14	1993–2014	4 / month	61 days	15
<b>ISAC</b>	1.5°×1.5°	Fixed	06/08/17	1981–2010	Every 5 days	32 days	5
<b>KMA</b>	1.5°×1.5°	On the fly	2019	1991–2010	4 / month	60 days	3
<b>NCEP</b>	1.5°×1.5°	Fixed	03/01/11	1999–2010	Daily	44 days	4
<b>UKMO</b>	1.5°×1.5°	On the fly	2019	1993–2016	4 / month	60 days	7
<b>HMCR</b>	1.5°×1.5°	On the fly	2019	1985–2010	Every 7 days	61 days	10
<b>ECMWF</b>	1.5°×1.5°	On the fly	2019	1999–2018	2 / week	46 days	11
<b>CMA</b>	1.5°×1.5°	On the fly	2019–2020	2005–2018	2 / week	60 days	4

832

833 **TABLE 1.** Characteristics of the nine forecast models within the S2S Reforecast Database that  
834 are utilized as part of this study.

835

836

837

838

839

840

841

842

843

844

845

846

847

848

849

850

851

852

853

854

855

856

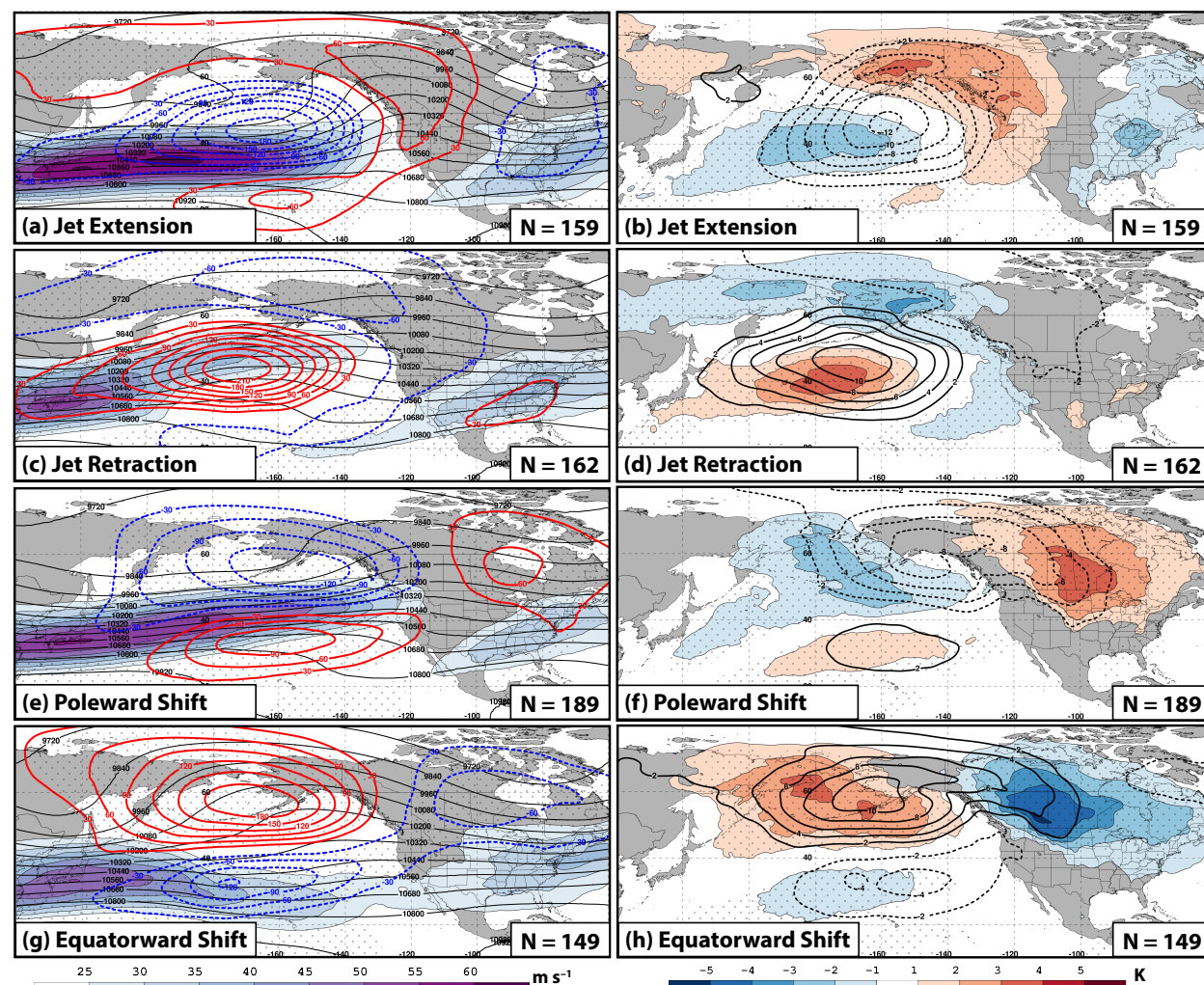


**FIG. 1.** Composite mean 250-hPa wind speed (shaded according to the fill pattern;  $\text{m s}^{-1}$ ), 250-hPa geopotential height (contoured in black every 120 m), and 250-hPa geopotential height anomalies (contoured every 30 m in red where positive and in dashed blue where negative) 4 days following the initiation of (a) a jet extension, (c) a jet retraction, (e) a poleward shift, and (g) an equatorward shift NPJ regime. Composite anomalies of mean sea-level pressure (contoured every 2 hPa in solid black where positive and in dashed black where negative) and 850-hPa temperature (shaded according to the legend every 1 K) 4 days following the initiation of (b) a jet extension, (d) a jet retraction, (f) a poleward shift, and (h) an equatorward shift NPJ regime. The numbers in the bottom right of each panel indicate the number of cases included in each composite. Stippled areas represent locations where the 250-hPa geopotential height anomalies or 850-hPa temperature anomalies are statistically distinct from climatology at the 99% confidence level based on a two-sided Student's  $t$  test. Figure and caption adapted from Winters et al. (2019a; their Fig. 5). © American Meteorological Society. Used with permission.

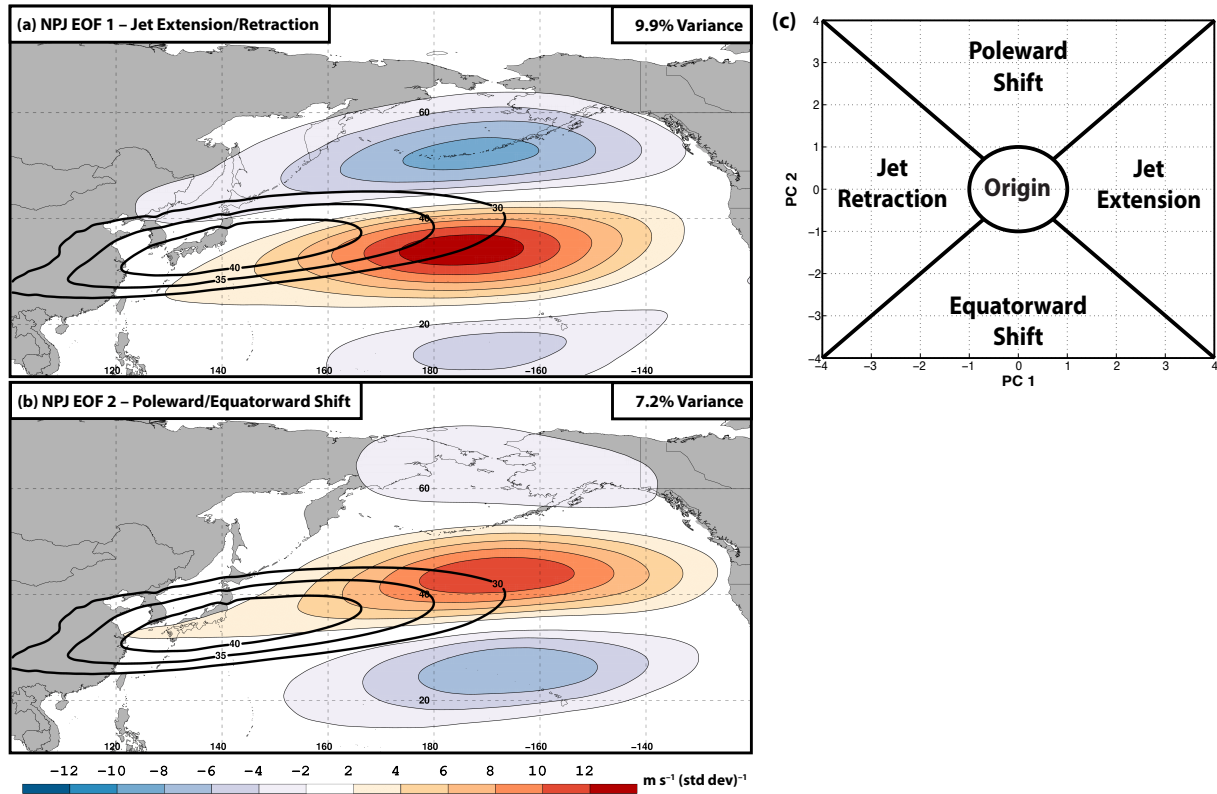


**FIG. 2.** September–May 300-hPa mean zonal wind is contoured in black every  $5 \text{ m s}^{-1}$  above  $30 \text{ m s}^{-1}$ , and the regression of 300-hPa zonal wind anomaly data onto standardized PC 1 (i.e., EOF 1) is shaded. The variance of 300-hPa zonal wind anomalies during September–May that is explained by EOF 1 is listed in the top right of the panel. (b) As in (a), but for the regression of 300-hPa zonal wind anomaly data onto standardized PC 2 (i.e., EOF 2). (c) Schematic depicting the NPJ phase diagram and the method used to classify the NPJ into an NPJ regime.

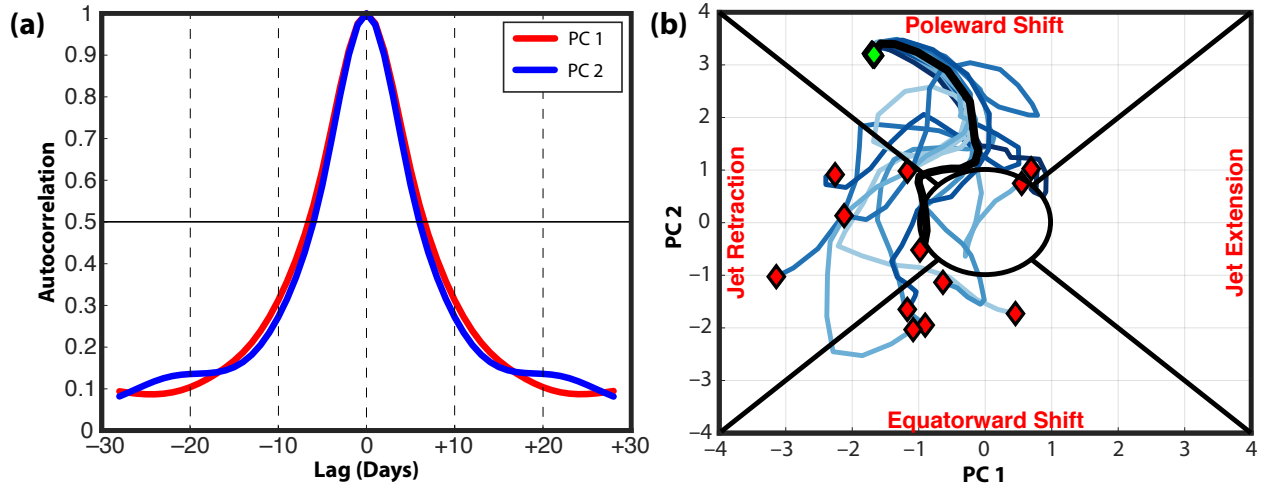


**FIG. 3.** (a) Autocorrelation functions for PC 1 and PC 2 that are derived from an EOF analysis of 300-hPa zonal wind anomalies over the North Pacific during September–May within the CFSR. The thin horizontal black line corresponds to an autocorrelation of 0.5. (b) A sample 21-day NPJ phase diagram ensemble forecast initialized at 0000 UTC 4 February 1999. Blue lines correspond to individual ensemble member forecasts and the thick black line corresponds to the ensemble mean forecast. The green diamond identifies the state of the NPJ at the time of forecast initialization and red diamonds identify the state of the NPJ at the end of the 21-day forecast period for each ensemble member and the ensemble mean.

895

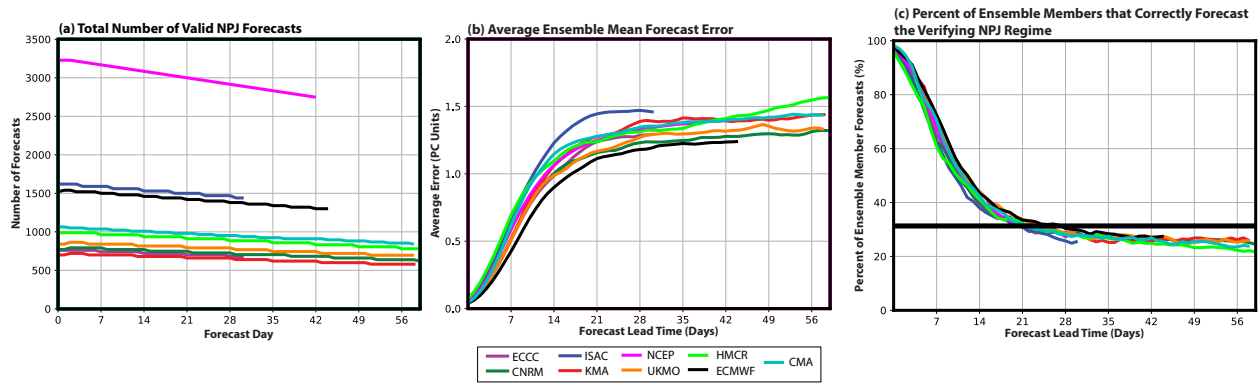


**FIG. 4.** (a) The total number of valid NPJ phase diagram forecasts initialized by each model at each forecast lead time. (b) The average Euclidean distance error (in principal component (PC) units) of ensemble mean NPJ phase diagram forecasts from each model as a function of forecast lead time. (c) The percent of ensemble member forecasts initialized from each model that correctly forecasted the verifying NPJ regime as a function of forecast lead time. The horizontal black bar identifies percentages that are statistically significant at the 99% confidence interval compared to random chance based on a bootstrap resampling test with replacement.



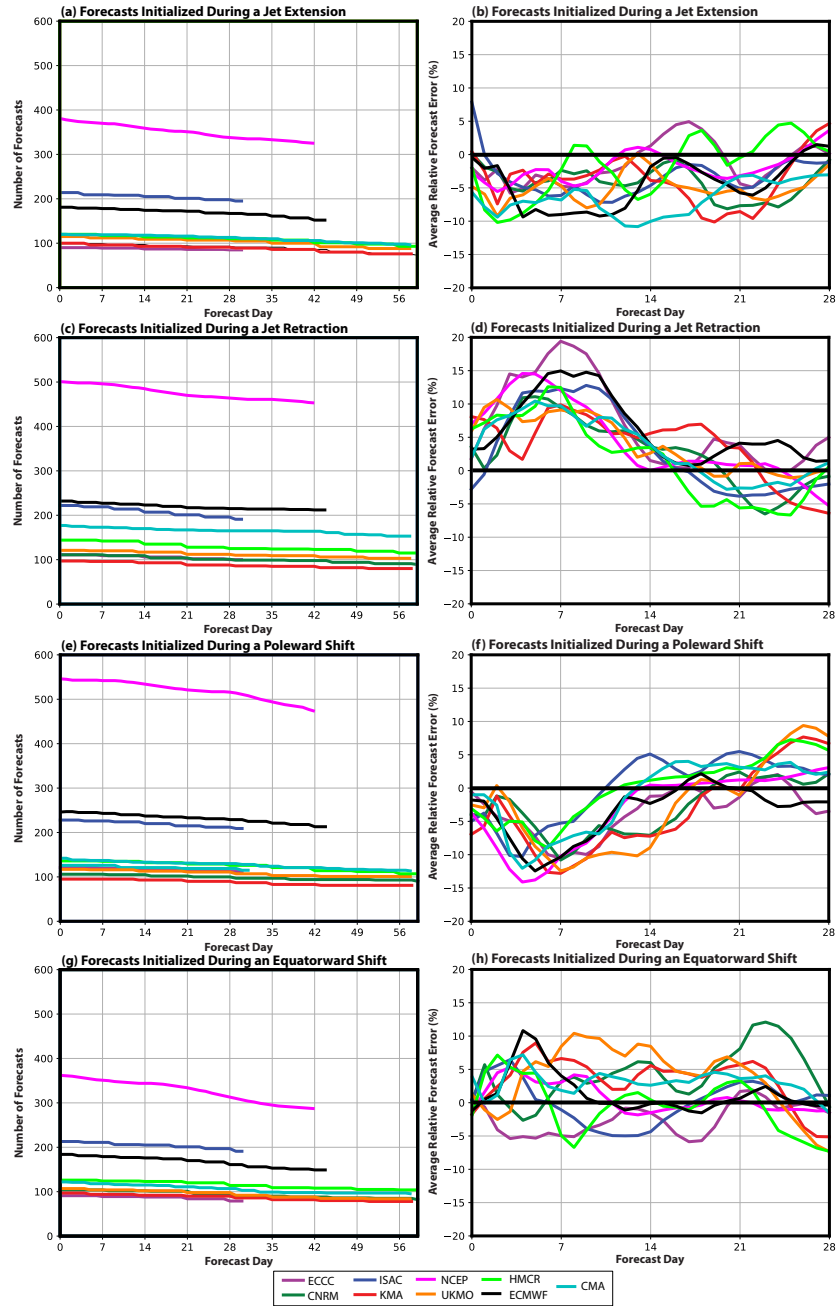


**FIG. 5.** The number of NPJ phase diagram forecasts from each model that were initialized during (a) a jet extension, (c) a jet retraction, (e) a poleward shift, and (g) an equatorward shift as a function of forecast lead time. The average Euclidean distance error of ensemble mean NPJ phase diagram forecasts from each model that were initialized during (b) a jet extension, (d) a jet retraction, (f) a poleward shift, and (h) an equatorward shift. All forecast model errors in (b,d,f,h) are expressed as a percentage greater or less than the average error of all NPJ phase diagram forecasts from that model that were initialized within one of the four primary NPJ regimes.

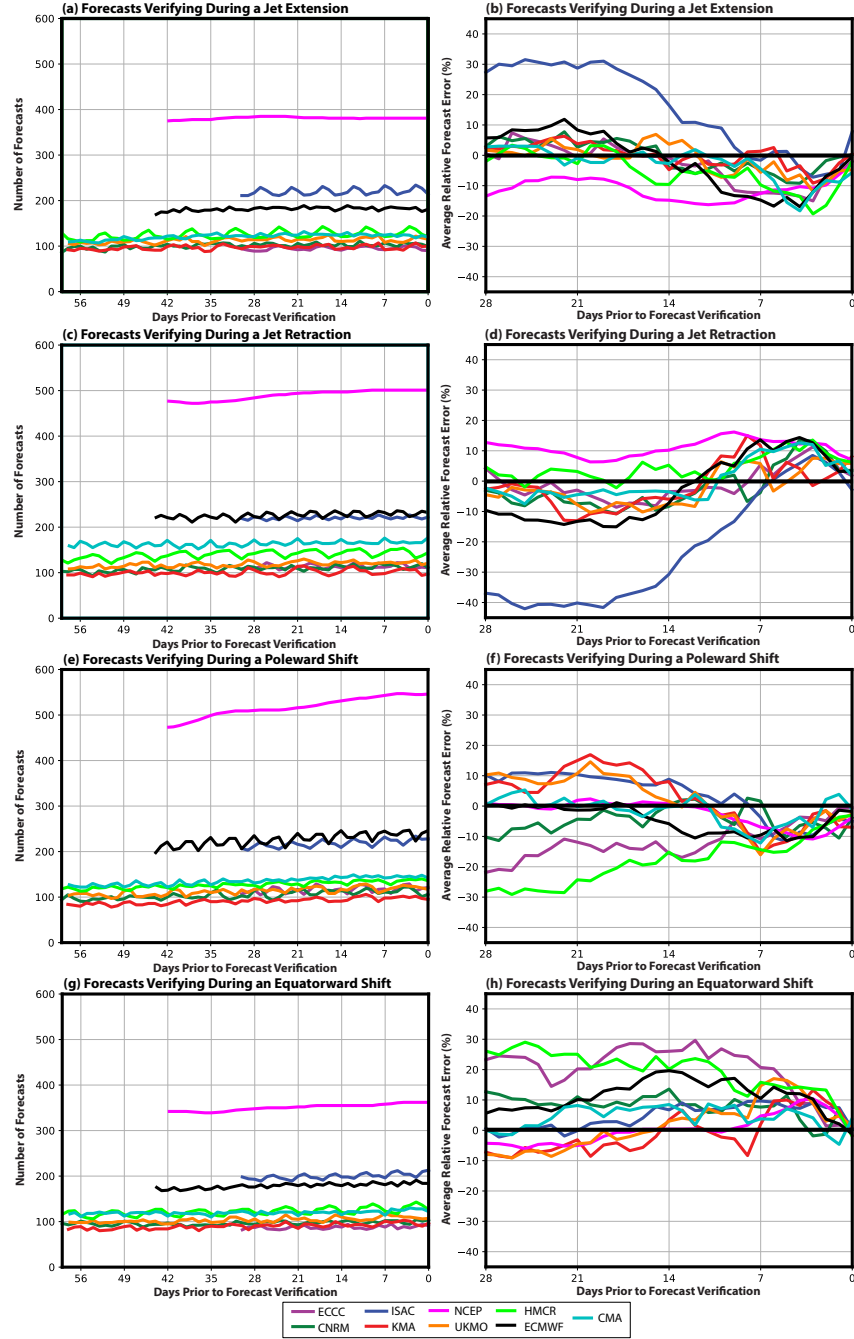


**FIG. 6.** The number of NPJ phase diagram forecasts from each model that verified during (a) a jet extension, (c) a jet retraction, (e) a poleward shift, and (g) an equatorward shift as a function of forecast lead time prior to verification. The average Euclidean distance error of ensemble mean NPJ phase diagram forecasts from each model that verified during (b) a jet extension, (d) a jet retraction, (f) a poleward shift, and (h) an equatorward shift. All forecast model errors in (b,d,f,h) are expressed as a percentage greater or less than the average error of all NPJ phase diagram forecasts from that model that verified within one of the four primary NPJ regimes.

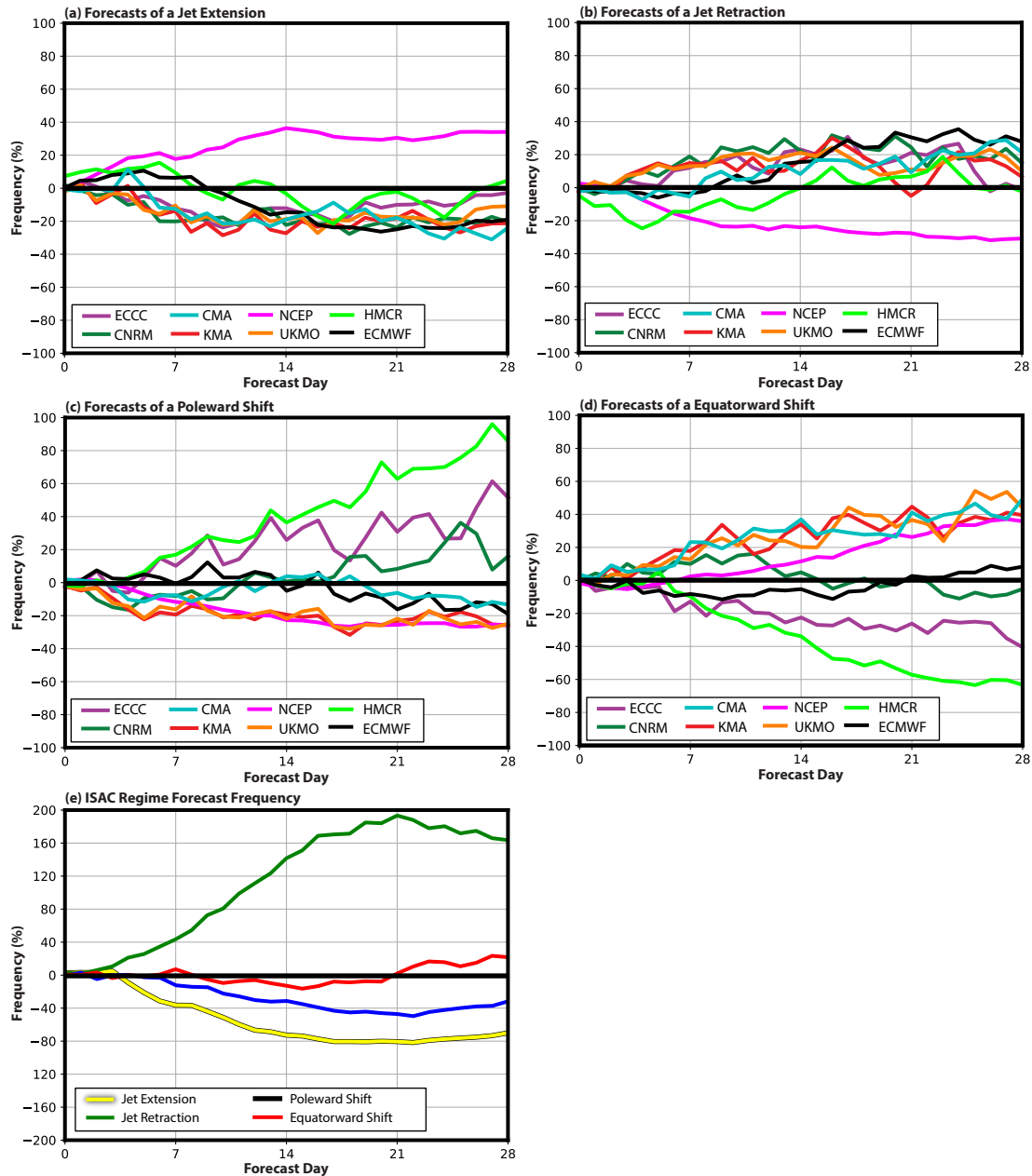


**FIG. 7.** The percent frequency that (a) a jet extension, (b) a jet retraction, (c) a poleward shift, and (d) an equatorward shift is overforecast (positive percentages) or underforecast (negative percentages) by ensemble member NPJ phase diagram forecasts from each model relative to verification at every forecast lead time. (e) The percent frequency that each NPJ regime is overforecast or underforecast relative to verification at each forecast lead time for the ISAC model.

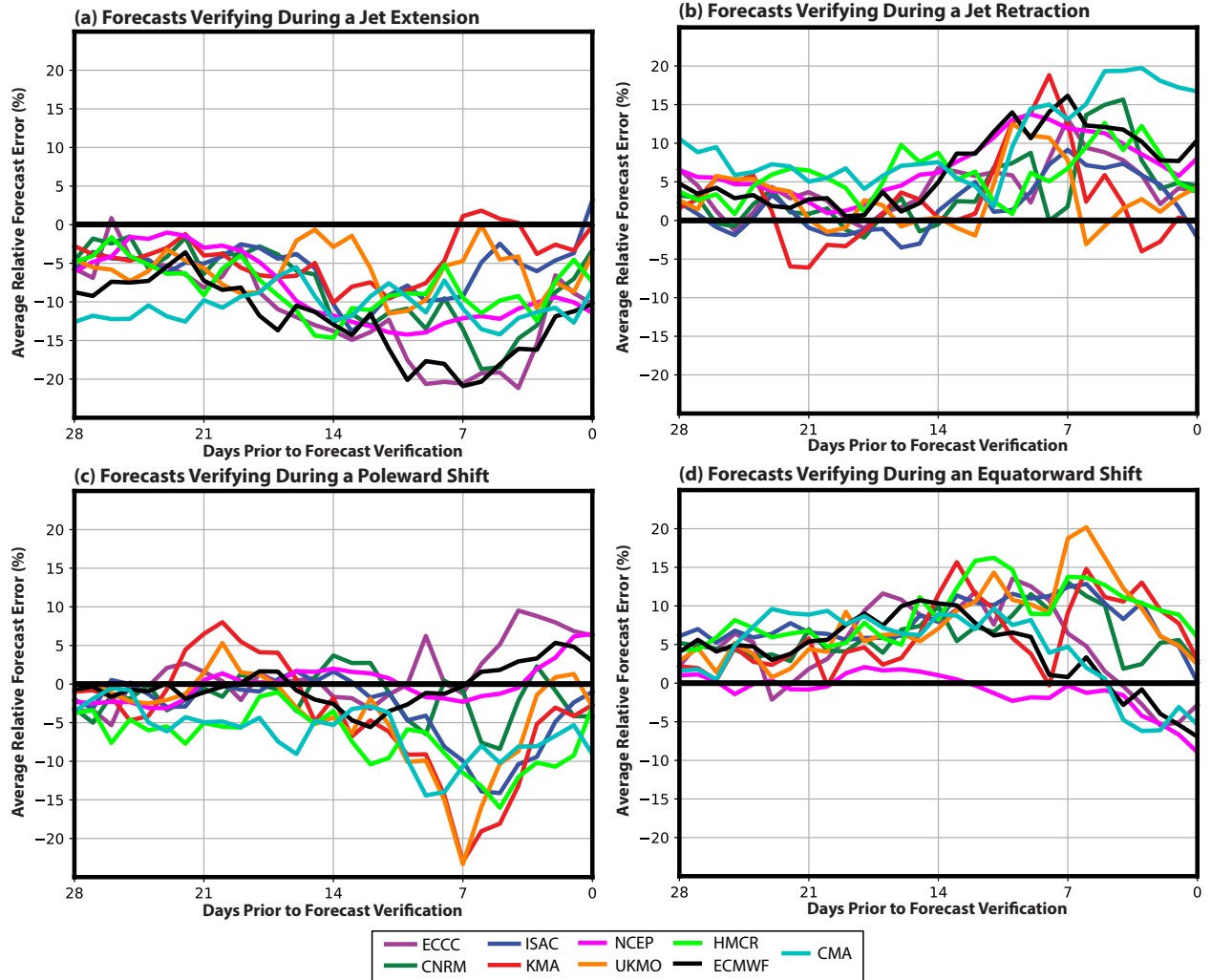


**FIG. 8.** As in Figs. 6b,d,f,h, but showing the errors associated with bias-corrected NPJ phase diagram forecasts from each model as a function of forecast lead time for forecasts that verify during (a) a jet extension, (b) a jet retraction, (c) a poleward shift, and (d) an equatorward shift.

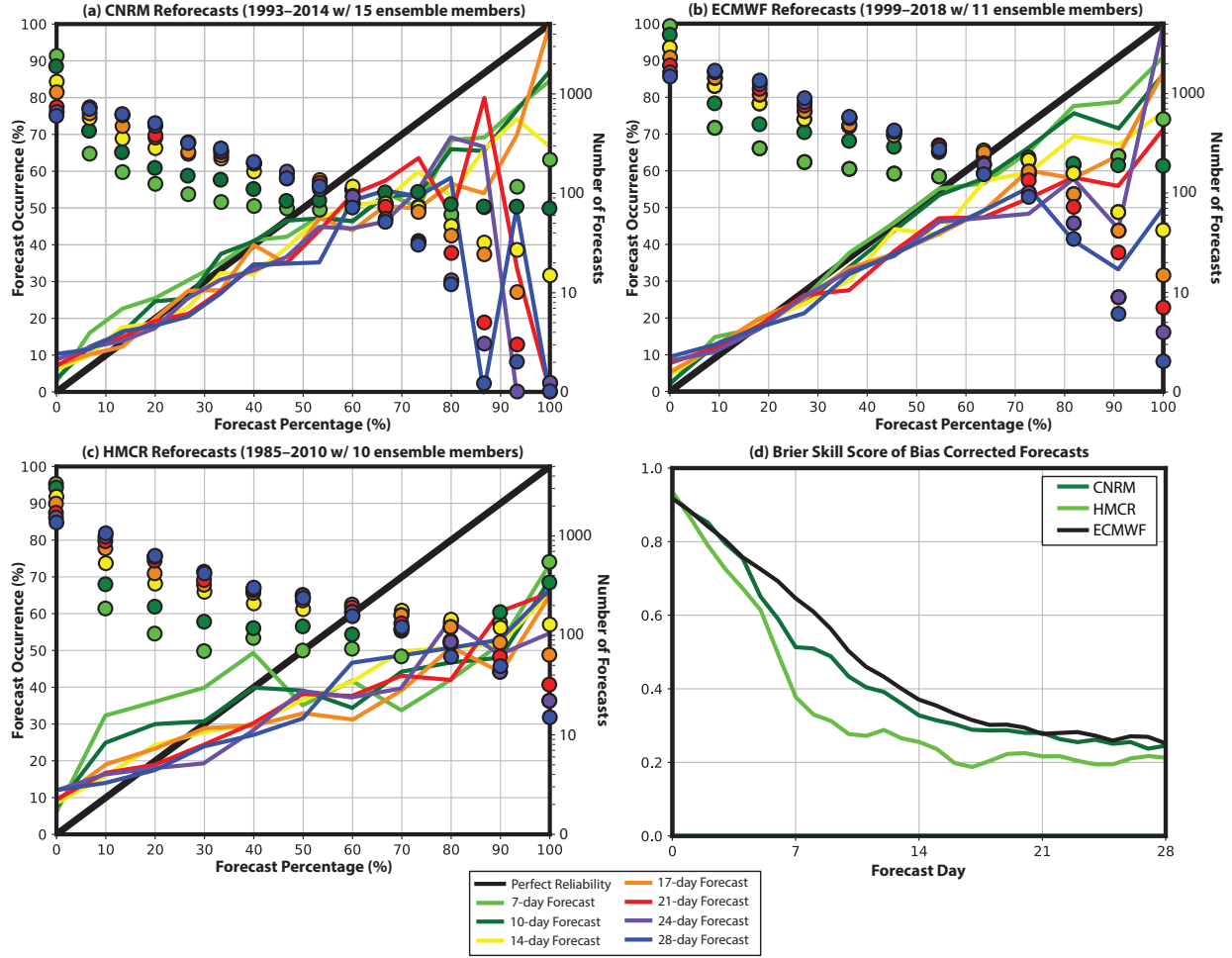


**FIG. 9.** Reliability diagrams at a variety of forecast lead times for the (a) CNRM, (b) ECMWF, and (c) HMCR bias-corrected ensembles. Shown in these diagrams are the probability that a particular NPJ regime is forecast to occur at a given lead time versus the percent of time that the forecasted NPJ regime verified. The thick black line represents a perfectly reliable forecast, and the colored dots show the number of forecasts within each probabilistic bin on a log scale as a function of forecast lead time. (d) The Brier Skill Scores associated with CNRM, HMCR, and ECMWF probabilistic forecasts as a function of forecast lead time.

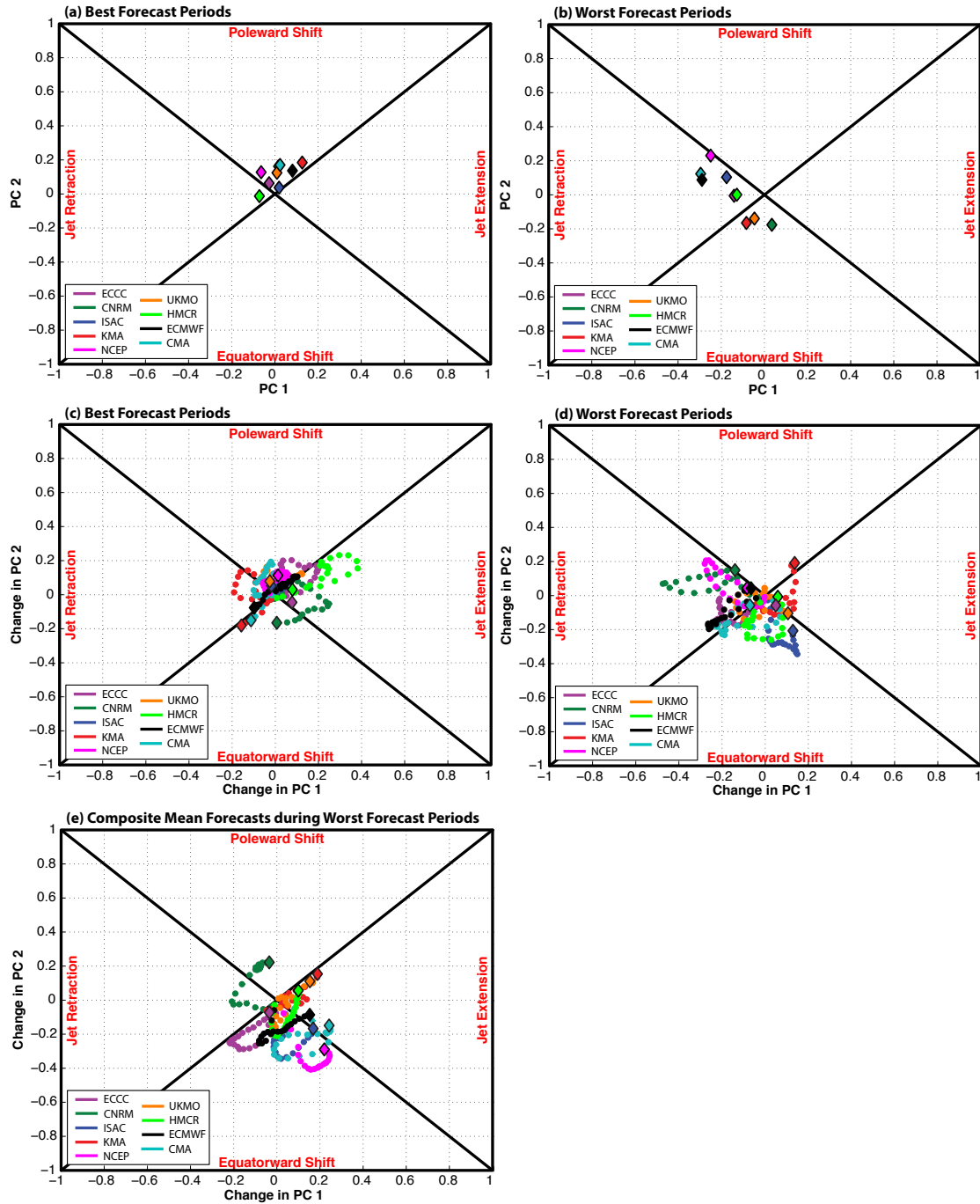


**FIG. 10.** The average position of the NPJ within the NPJ phase diagram at the time (a) a best-performing forecast and (b) a worst-performing forecast is initialized from each model. Trajectories showing the composite evolution of the NPJ within the NPJ phase diagram during the 21-day period after the initiation of (c) a best-performing forecast and (d) a worst-performing forecast from each model. (e) The composite ensemble mean 21-day forecast trajectories constructed from the worst-performing NPJ phase diagram forecasts from each model.

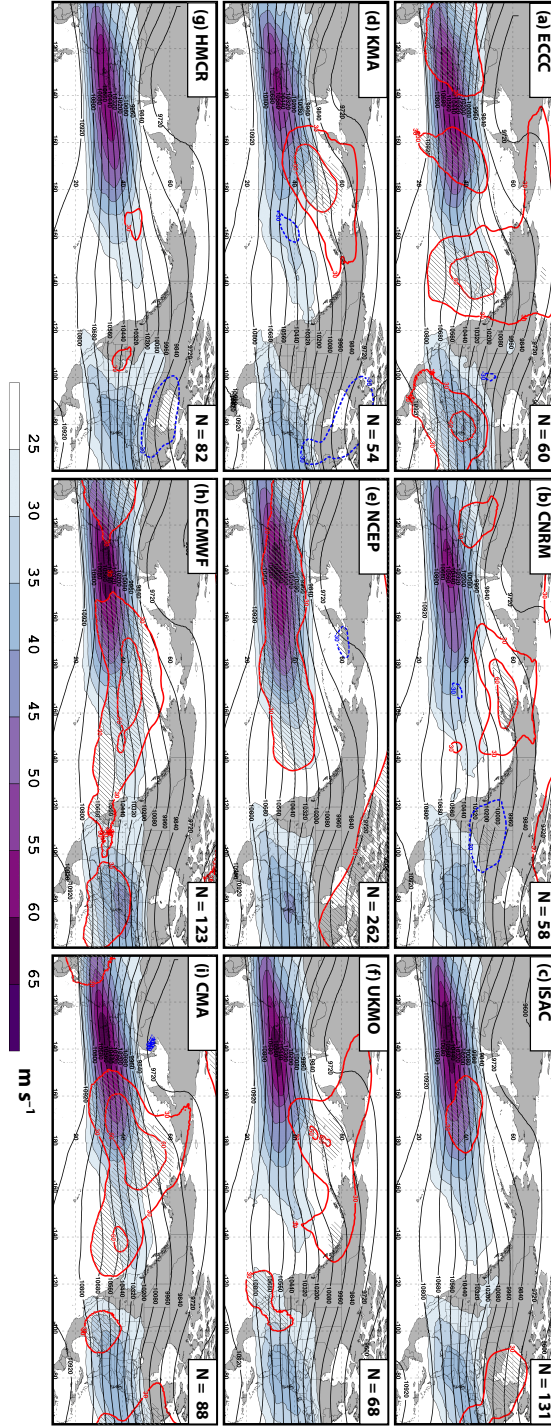


**FIG. 11.** Composite mean 250-hPa wind speed (shaded according to the fill pattern;  $\text{m s}^{-1}$ ), 250-hPa geopotential height (contoured in black every 120 m), and 250-hPa geopotential height anomalies (contoured every 30 m in red where positive and in dashed blue where negative) from the CFSR at the time a worst-performing forecast is initialized from the (a) ECCC, (b) CNRM, (c) ISAC, (d) KMA, (e) NCEP, (f) UKMO, (g) HMCRC, (h) ECMWF, and (i) CMA model. Hatched regions indicate geopotential height anomalies that are statistically distinct from climatology at the 95% confidence interval using a two-sided Student's  $t$  test.



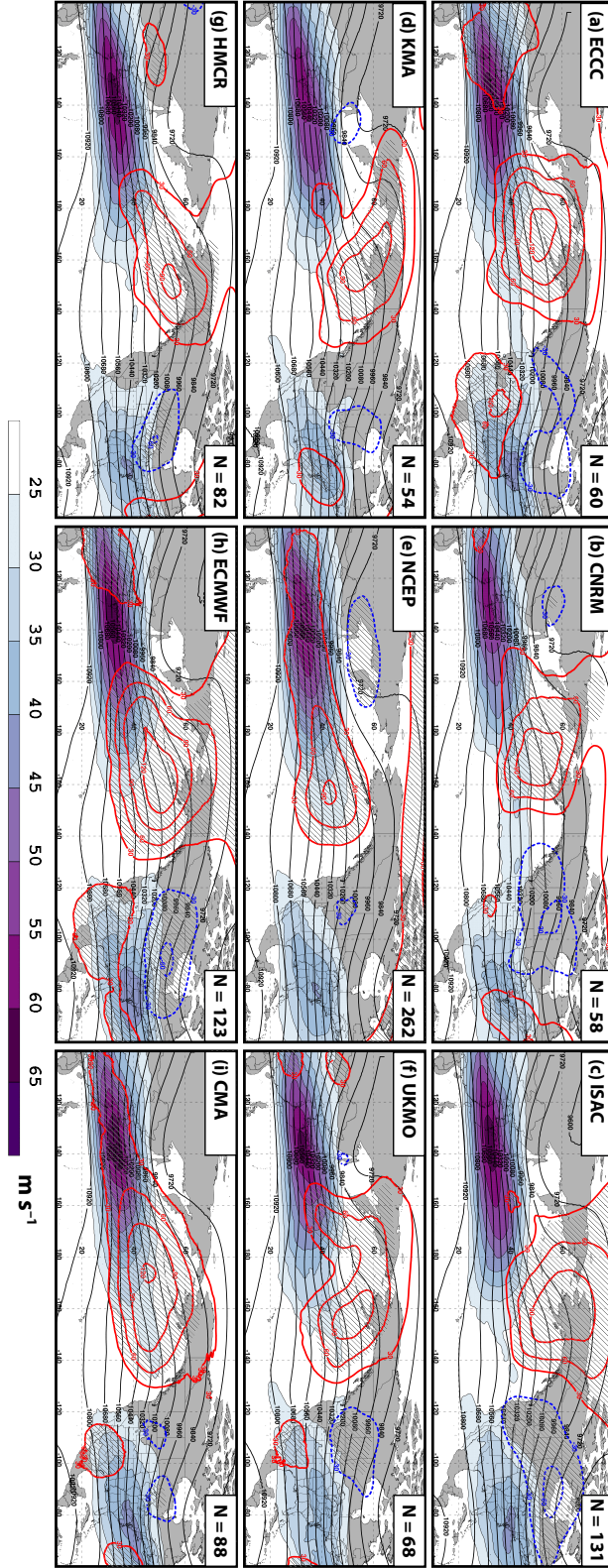


**FIG. 12.** As in Fig. 11, but showing composites from the CFSR 10 days after the initialization of a worst-performing forecast from each model.



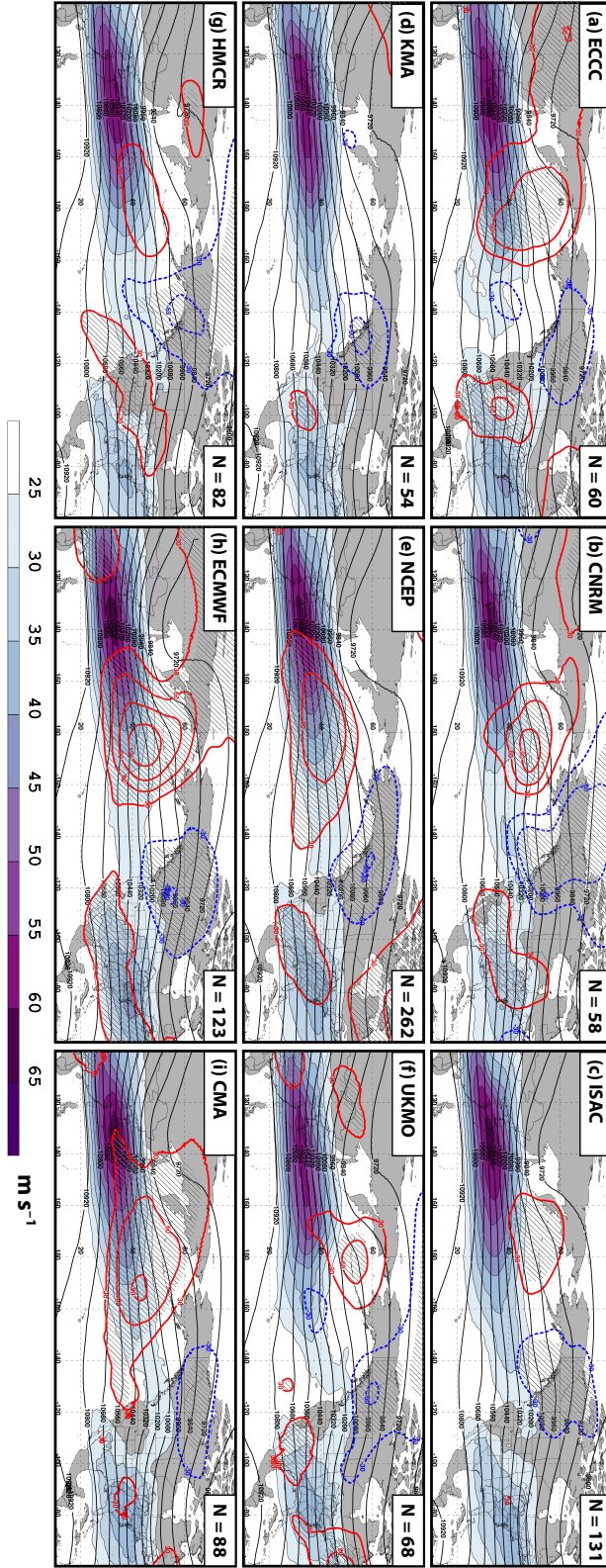


**FIG. 13.** As in Fig. 11, but showing composites from the CFSR 20 days after the initialization of a worst-performing forecast from each model.

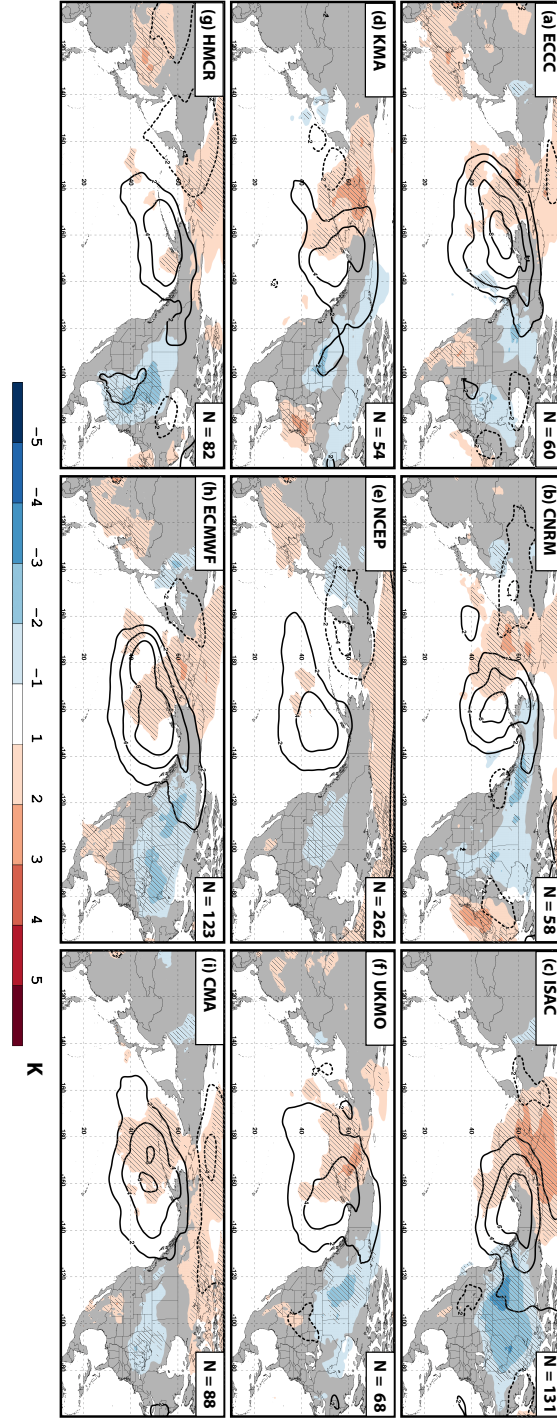


**FIG. 14.** Composite mean 850-hPa temperature anomalies (shaded according to the legend every 1 K), and mean sea-level pressure anomalies (contoured every 2 hPa in solid black where positive and in dashed black where negative) from the CFSR 10 days after a worst-performing forecast is initialized from the (a) ECCC, (b) CNRM, (c) ISAC, (d) KMA, (e) NCEP, (f) UKMO, (g) HMCR, (h) ECMWF, and (i) CMA model. Hatched regions indicate 850-hPa temperature anomalies that are statistically distinct from climatology at the 95% confidence interval using a two-sided Student's  $t$  test.